

Energy Spectrum of $^{12}\text{B}/^{12}\text{N}$ Beta
Decays from the RENO Experiment
and Production of Microscopic Black
Holes in 100TeV proton collision.

Nackyoung Yang

The Graduate School
SungKyunKwan University
Department of Physics

Energy Spectrum of $^{12}\text{B}/^{12}\text{N}$ Beta
Decays from the RENO Experiment
and Production of Microscopic Black
Holes in 100TeV proton collision.

Nackyoung Yang

A master Thesis Submitted to the Department of
Physics and the Graduate School of SungKyunKwan
University in partial fulfillment of the requirements for
the degree of Master of Science

Contents

Part I

1. Introduction	1
1.1 Neutrino Oscillation	1
1.2 Reactor Neutrino Experiment	2
1.3 Beta Decay of $^{12}\text{B}/^{12}\text{N}$	3
1.3.1 Muon induced Isotopes in RENO	3
1.3.2 ^{12}B β^- Decay	4
1.3.3 ^{12}N β^+ Decay	4
2. RENO Experiment	6
2.1 Overview	6
2.2 Experimental Arrangement	
2.2.1 Near and Far Detectors	8
2.3 Detector Components	9
2.3.1 Target and Gamma Catcher	10
2.3.2 Buffer	10
2.3.3 Veto	10
2.3.4 PMT	11
3. Data Selection	12
3.1 Production of $^{12}\text{B}/^{12}\text{N}$ in the RENO	12
3.2 Prompt Muon Signal Selection	12
3.2.1 Muon Energy Cut	12

3.3	Radioactive isotope candidate selection	12
3.3.1	Time Selection for Signal Time Window	12
3.3.2	Time Selection for Background Time Window	13
3.3.3	^{12}B and ^{12}N Candidate Energy Cut	13
3.3.4	Vertex Cut	13
3.3.5	Flasher Cut	13
3.4	Data Set	14
3.5	Final selection criteria	15
4.	Monte-Carlo Simulation	15
4.1	Beta decay spectrum	15
4.2	Event generation for ^{12}B and ^{12}N β -decay	17
4.3	MC selection	18
5.	Energy Calibration	18
5.1	Energy Calibration System	19
5.2	Energy Conversion Function	20
6.	Measurement of the energy spectrum of ^{12}B and ^{12}N β -decays	22
6.1	Fitting Method to Measure ^{12}B / ^{12}N Spectrum	22
6.2	^{12}B / ^{12}N Energy Spectrum	24
7.	Summary	28

Part II

8.	Production of Microscopic Black Holes	29
8.1	BLACK HOLES AT THE LHC	29
8.1.1	Black hole production in particle collision	29
8.1.2	The production cross section in a pp collision	31
8.1.3	Black hole decay by Hawking radiation	32
9.	CHARYBDIS II Monte-Carlo simulation	32
9.1	CHARYBDIS II: A Black Hole Event Generator	32
9.2	Incorporation of the results into CHARYBDIS2	33
9.2.1	BLACK HOLE PRODUCTION CROSS SECTION	33
9.2.2	5D wave functions	33
9.2.3	Cross section	34
9.2.4	C – factor	34
10.	Study of microscopic black holes in 100TeV p - p collisions	36
10.1	Black hole in the Randall-Sundrum model and ADD model	36
10.2	ADD black hole and RS black hole	36
10.3	100TeV colliders' safety in the context of stable micro black holes production	37
11.	Summary	40

Part I

1. Introduction

1.1 Neutrino Oscillation

The observation of neutrino oscillation is one of the most important discoveries in particle physics. Neutrino oscillation is a flavor transformation of a neutrino from one type to another. Neutrino oscillation and nonzero neutrino masses provides insights into the current standard model.

Neutrino oscillation is a consequence of the neutrino flavor being linear combination of the mass eigenstates. The currently accepted model describing neutrino mixing is a framework of three flavors (ν_e, ν_μ, ν_τ) characterized by three mixing angles ($\theta_{12}, \theta_{23}, \theta_{13}$), three mass difference ($\Delta m_{21}^2, \Delta m_{22}^2, \Delta m_{31}^2, \Delta m_{32}^2$), and one phase angle (δ). In 1998, the Super-Kamiokande experiment discovered neutrino oscillation in atmospheric neutrinos and measured the mixing angle θ_{23} for the first time. It is interesting that angle θ_{23} is close to the maximal value. The solar neutrino oscillation was discovered by the SNO collaboration in 2001, and the mixing angle θ_{12} was also measured. Both experiments were awarded the Nobel prize in Physics in 2015 for the discovery of the neutrino oscillations.

*add
reference*

The last unknown angle, the smallest mixing angle θ_{13} , was finally measured in 2012 by the RENO, Daya Bay and Double-Chooz experiments via the electron anti-neutrino disappearance from reactor. These reactor neutrino experiments could measure θ_{13} without matter effects and charge parity (CP) violation. The first measurement of θ_{13} by RENO was based on the rate-only analysis to compare expected and observed reactor neutrino rates. In 2016, the RENO collaboration published a more precise measurement of θ_{13} and the first measurement of $|\Delta m_{ee}^2|$, a mixture of $|\Delta m_{31}^2|$ and $|\Delta m_{32}^2|$, obtained from energy and baseline dependent disappearance of reactor electron antineutrinos.

✓

A neutrino with flavor α and momentum \vec{p} is a combination of different mass eigenstates. Mathematically

$$|\nu_\alpha\rangle = \sum_i U_{\alpha i}^* |\nu_i\rangle \quad (1.1)$$

The mass eigenstates are eigenstates of the hamiltonian. This implies the mass eigenstates can evolve in time as plane waves.

$$|\nu_\alpha(t)\rangle = \sum_i U_{\alpha i}^* e^{-iE_i t} |\nu_i\rangle \quad (1.2)$$

✓

inverting equation(1.1), the neutrino flavor states can be expressed in terms of other flavor states.

$$|\nu_\alpha(t)\rangle = \sum_{\beta=e,\mu,\tau} U_{\alpha i}^* e^{-iE_i t} U_{\beta i} |\nu_\beta\rangle \quad (1.3)$$

Therefore, The transition probability of ν_α to ν_β ($\alpha, \beta = e, \mu, \tau$) with energy E after traveling distance L in vacuum can be calculated as follows:

$$P(\nu_\alpha \rightarrow \nu_\beta) = |\langle \nu_\alpha | \nu_\beta \rangle|^2 \quad (1.4)$$

$$= \delta_{\alpha\beta} - 2\text{Re} \sum_{j>i} U_{\alpha i} U_{\alpha j}^* U_{\beta i}^* U_{\beta j} \left(1 - \exp \left\{ i \Delta m_{ji}^2 L \frac{2}{E} \right\} \right)$$

Where $\Delta m_{ji}^2 \equiv m_j^2 - m_i^2$ is the difference between the neutrino masses squared. If the neutrino has 3 flavors and 3 mass eigenstates, matrix U is described by a 3×3 matrix which is called Pontecorvo-Maki-Nakagawa-Sakata (PMNS) matrix.

$$U = \begin{pmatrix} 1 & 0 & 0 \\ 0 & c_{23} & s_{23} \\ 1 & -s_{23} & c_{23} \end{pmatrix} \begin{pmatrix} c_{13} & 0 & s_{13}e^{i\delta} \\ 0 & 1 & 0 \\ -s_{13}e^{-i\delta} & 0 & c_{13} \end{pmatrix} \begin{pmatrix} c_{12} & s_{12} & 0 \\ -s_{12} & c_{12} & 0 \\ 0 & 0 & 1 \end{pmatrix} \quad (1.5)$$

$$= \begin{pmatrix} c_{12}c_{13} & s_{12}c_{13} & s_{13}e^{-i\delta} \\ -s_{12}c_{23} - c_{12}s_{23}s_{13}e^{i\delta} & c_{12}c_{23} - s_{12}s_{23}s_{13}e^{i\delta} & s_{23}c_{13} \\ s_{12}s_{23} - c_{12}c_{23}s_{13}e^{i\delta} & -c_{12}s_{23} - s_{12}c_{23}s_{13}e^{i\delta} & c_{23}c_{13} \end{pmatrix}$$

Where $c_{ij} = \cos \theta_{ij}$, $s_{ij} = \sin \theta_{ij}$ (θ_{ij} is the mixing angle), and δ is a Dirac CP violating phase. A further theoretical description of neutrino mixing can be found in Ref. [1]. The current best values of neutrino oscillation parameters with errors of one standard deviation (1σ) are summarized as follows: Ref. [2]

$$\sin^2 2\theta_{23} = 0.999_{-0.018}^{+0.001} \text{ (normal)} \left[\begin{matrix} +0.1\% \\ -1.8\% \end{matrix} \right] \quad (1.6)$$

$$\text{or } 1.000_{-0.017}^{+0.000} \text{ (inverted)} \left[\begin{matrix} +0.0\% \\ -1.7\% \end{matrix} \right]$$

$$\sin^2 2\theta_{12} = 0.846 \pm 0.021 [\pm 2.5\%]$$

$$\sin^2 2\theta_{13} = 0.093 \pm 0.008 [\pm 8.6\%]$$

$$\Delta m_{32}^2 = (2.44 \pm 0.06) \times 10^{-3} \text{ eV}^2 \text{ (normal)} [\pm 2.5\%]$$

$$\text{or } (2.52 \pm 0.07) \times 10^{-3} \text{ eV}^2 \text{ (inverted)} [\pm 2.8\%]$$

$$\Delta m_{21}^2 = (7.53 \pm 0.18) \times 10^{-5} \text{ eV}^2 [\pm 2.4\%]$$

Where, the bracketed values are the fractional errors. Note that disappearance experiments cannot measure the sign of Δm_{32}^2 because the dominant term in the Equation (1.6) depends on the square of the sine function. This is called the neutrino mass hierarchy problem.

1.2 Reactor Neutrino Experiment

Past reactor experiments could not observe neutrino disappearance using a single detector located ~ 1 km or less from the reactor. To measure the rate and energy spectrum of the $\bar{\nu}_e$ s,

CHOOZ and Palo Verde used a single detector with ~ 1 km baseline. Such measurements from the single detector are sensitive to systematic issues related to the detector and the reactors. To avoid this problem, current experiments such as Daya Bay, Double Chooz, and RENO are deploying multiple identical detectors at different distances in relation to the reactors, which allows the disappearance of $\bar{\nu}_e$ to be obtained from the ratio of the observed $\bar{\nu}_e$ rates at each detector. Because it is a relative measurement, the far-to-near ratio can significantly reduce the systematic uncertainties from the detector and reactor. In 2012, the two reactor disappearance experiments - Daya Bay and RENO reported the first measurement of the θ_{13} value. The measurement of θ_{13} by the RENO was based on the rate-only analysis on anti-electron neutrino deficit. In the updated analysis published in 2016, a more precisely measured value of θ_{13} was reported, based on the rate, spectral, and baseline information of reactor neutrino disappearance (rate + shape analysis). Using shape information of reactor neutrino energy spectrum, it was possible to measure the value of θ_{13} with less systematic error than that of the rate only analysis. Because the spectral shape of the backgrounds is different from that of the reactor neutrino, it is easy to distinguish between the backgrounds and the neutrino.

1.3 Beta Decay of $^{12}\text{B}/^{12}\text{N}$

When muons from cosmic rays pass through the Gd-LS, they generate both Cherenkov and scintillation light. Also, secondary particles generated by muon spallation or EM shower could interact with carbon nuclei and produce radioactive isotopes. Table 1.1 shows the list of radioactive isotopes from muon spallation.

Isotope	^{12}B	^{12}N	^9Li	^8He	^9C
Half-life	20.20ms	11ms	178.3ms	119.0ms	126.5ms
Q Value (MeV)	13.370	17.338	13.606	10.652	16.497

Table 1.1

1.3.1 Muon induced Isotopes in RENO

According former research [31], the process for generating ^{12}B and ^{12}N could be:



And also ^{12}B and ^{12}N could be generated inside detectors by the following process:



These radioactive isotopes would undergo the beta decay process, in which the emission of electron or positron could be captured by a detector. The ^{12}B and ^{12}N beta decay processes are listed below.



order references

$$^{12}\text{N} \rightarrow ^{12}\text{C}^* + e^+ + \nu_e \quad (1.12)$$

The ^{12}B and ^{12}N isotopes are expected to be produced abundantly inside the RENO detector and their energy spectra range from ~ 3 MeV to ~ 17 MeV. Neutrino signals in the RENO detector show the energy spectrum between 1 and 10 MeV. Therefore the ^{12}B and ^{12}N isotopes provide an excellent sample for the validation of the RENO energy calibration which is essential in the measurement of θ_{13} .

1.3.2 ^{12}B β^- Decay

The β decay modes for ^{12}B are listed in Table 1.2 and Figure 1.1 shows the beta decay scheme of ^{12}B . The dominant mode is from 1^+ state to 0^+ state and the Q value is 13.37 MeV. In this thesis, we consider only three dominant modes.

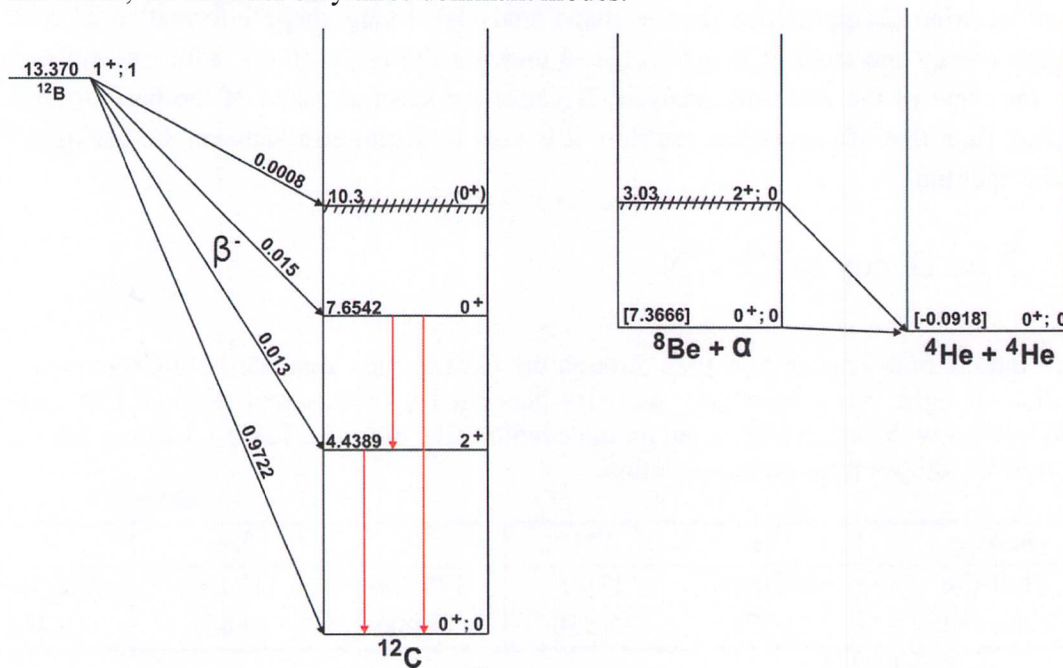


Figure 1.1: ^{12}B β^- decay scheme

$E_{\text{state}}(\text{MeV})$	Branching Ratio	$\Delta Spin$	$\Delta Parity$	N_{gamma}	$E_{\text{gamma}}(\text{MeV})$	Note
0	0.9722	1	0	0		β
4.4389	0.013	1	0	1	4.438	$\beta + \gamma$
7.6542	0.000255	1	0	2	3.2153, 4.4389	ignore
7.6542	0.01474	1	0	0		$\beta + \alpha$
10.3	0.0008	1	0	0		ignore

Table 1.2: ^{12}B ($A = 12$, $Z = 5$ and $Q = 13.370$ MeV) decay mode

1.3.3 ^{12}N β^+ Decay

text: ~~start beta~~ mention reason in small branching fraction

The β^+ decay mode for ^{12}N are listed in Table 1.3 and Figure 1.2 shows the beta decay scheme of ^{12}N . The dominant mode is from 1^+ state to 0^+ state and the Q value is 17.34 MeV. We take only the dominant mode into account for the analysis.

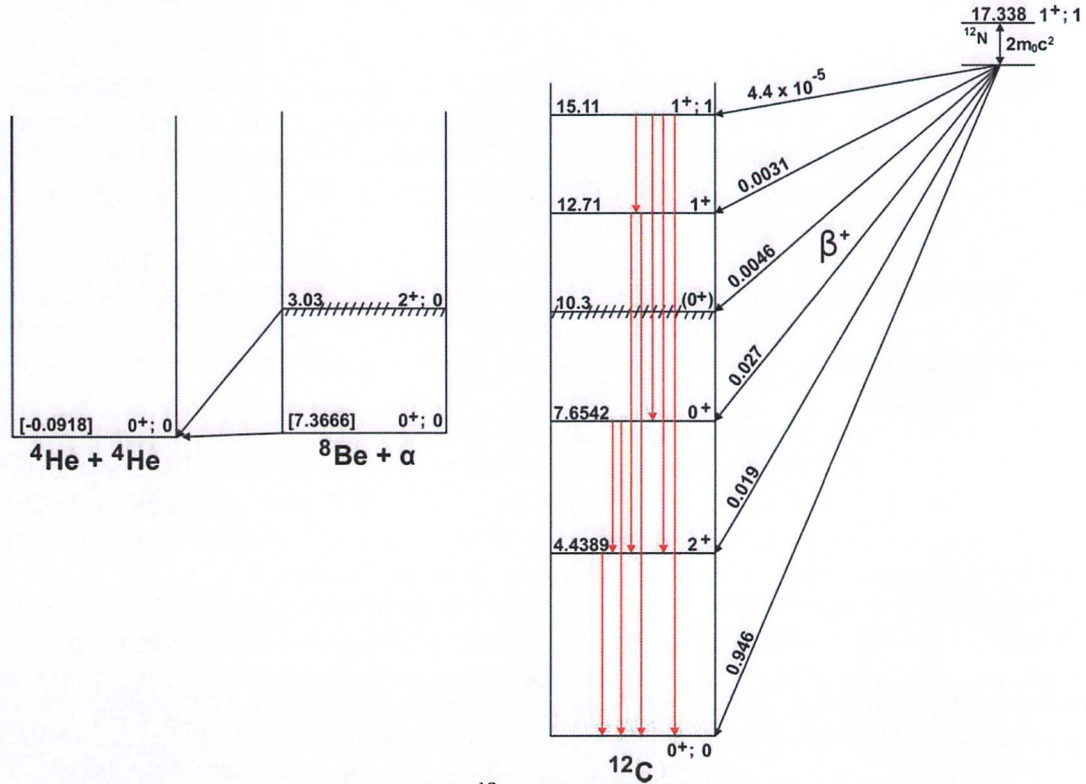


Figure 1.2: ^{12}N β^- decay scheme

$E_{\text{state}}(\text{MeV})$	Branching Ratio	$\Delta Spin$	$\Delta Parity$	N_{gamma}	$E_{\text{gamma}}(\text{MeV})$	Note
0	0.946	1	0	0		β
4.4389	0.019	1	0	1	4.438	$\beta + \gamma$
7.6542	0.000255	1	0	2	3.2153, 4.4389	ignore
7.6542	0.026745	1	0	0		$\beta + \alpha$
10.3	0.0046	1	0	0		$\beta + \alpha$
12.71	0.0031	1	0	0		ignore
15.11	0.000044	1	0	0		ignore

Table 1.3: ^{12}N ($A = 12$, $Z = 7$ and $Q = 17.338$ MeV) decay mode



2. RENO Experiment

2.1 Overview

The RENO is the experiment to measure the neutrino mixing angle θ_{13} using electron antineutrino emitted from the Hanbit nuclear power plant in Yonggwang, Korea with world-second largest thermal power output of 16.4 GW. The Hanbit site was chosen due to a large number of anti-neutrinos from the nuclear power plant at the site and a mountainous geography suitable for constructing underground detectors.

The RENO experiment has two identical detectors, one placed at ~ 294 m from the reactor array baseline and another at ~ 1384 m. They are called near detector and far detector, respectively. By using identical design for both detectors, a number of systematic uncertainties cancel out due to normalization of the neutrino flux at the far detector using that of the near detector.

The detectors have a layered structure similar to other reactor neutrino experiments, i.e. Daya Bay and Double Chooz experiments. The RENO detector consists of four cylindrical layers. They are, from the center, target, γ -catcher, buffer, and veto, where an outer layer almost enclosing an inner layer. The PMTs for detecting neutrino interaction will be in the buffer layer. The cutaway view of a RENO detector is shown in Fig. 2.1.

The "target" is gadolinium (Gd) doped liquid scintillator contained in a transparent cylindrical vessel made of acrylic plastic. An inverse beta decay event produces a positron and neutron pair. The positron loses energy through scintillating process before converted into two gammas via a pair annihilation. The neutron thermalizes and then is captured by Gd nucleus producing several gammas. The gammas produced close to the boundary of target can escape target without completely depositing its energy in scintillator. To contain the energy carried by gammas escaping from the target, the " γ -catcher," another liquid scintillator layer, surrounds target. Unlike the target, the liquid scintillator in the γ -catcher is not loaded with Gd since this layer is intended to augment the target in energy measurement of gammas emitted in target. As with target, a transparent cylindrical acrylic vessel contains γ -catcher liquid.

Surrounding the γ -catcher is a non-scintillating liquid layer called the "buffer." Mineral oil is used as the buffer medium and is contained in a cylindrical vessel made of stainless steel. The photomultiplier tubes (PMTs) are mounted on the inner surface of the buffer vessel immersed in buffer. The buffer acts as a shield against gammas mainly coming from radioactive isotope contained in PMTs entering the scintillating volume.

The outermost layer of the RENO detector is the "veto", a water Cherenkov detector layer. Its purpose is to reduce background gammas and neutrons from the surrounding environment (such as rocks) inner layers as well as rejecting cosmic muon induced background events. The veto container is constructed with 30 cm thick concrete and the top lid is made of stainless steel. PMTs are mounted on the inner surface of veto container for detecting Cherenkov light from cosmic muons.

The various design parameters have been determined for optimal performance using detailed simulation. The simulation includes backgrounds from PMTs and surrounding rocks, cosmic muons reaching the detector site as well as inverse beta decay from the reactor anti-neutrinos. The detector layers and vessels are summarized in Table 2.1.

Detector Component	Outer Diameter (mm)	Outer Height (mm)	Material	Volume (m ³)	Mass (tons)
Target	2750	3150	Gd-loaded LS	18.70	16.08
Target Vessel	2800	3200	Acrylic	33.19	1.18
γ -catcher	3940	4340	LS	2.38	28.55
γ -catcher Vessel	4000	4400	Acrylic	76.46	2.83
Buffer	5388	5788	Oil	1.05	64.22
Buffer Vessel	5400	5800	SUS	352.61	8.39
Veto	8388	8788	Water	352.61	352.61

Table 2.1: Dimensions of the mechanical structure of the detector.

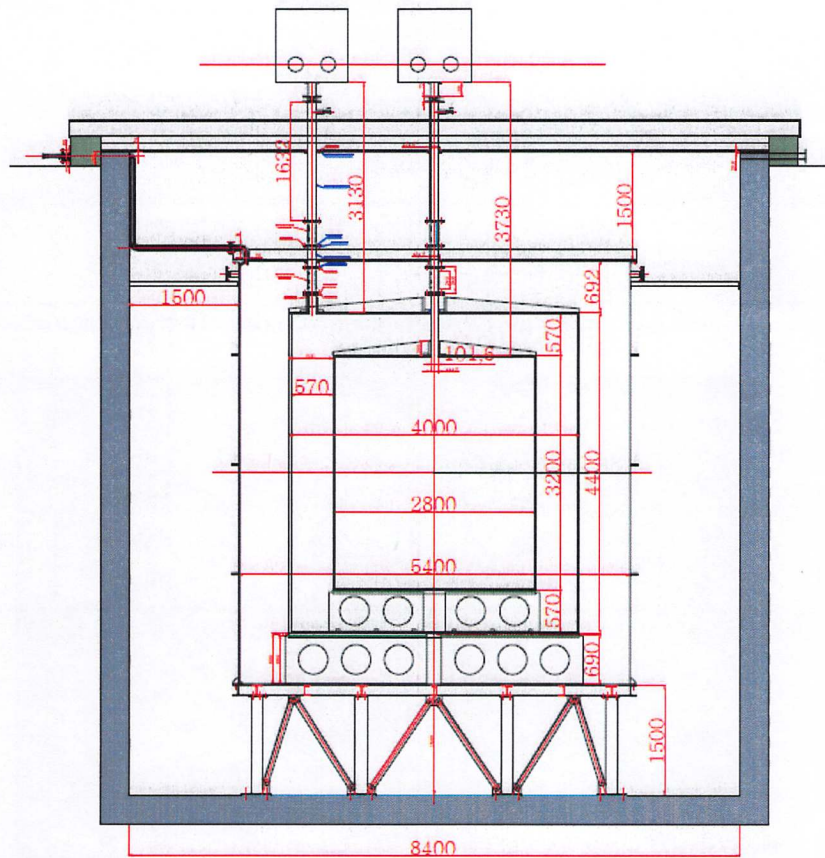


Figure 2.1: RENO detector. From the center, there are liquid scintillator filled target and gamma catcher with transparent acrylic vessel, mineral oil filled buffer with stainless steel vessel, and water filled veto layers. The PMTs for the inner and outer detectors are inwardly mounted on buffer and veto vessels, respectively.

2.2 Experimental Arrangement

2.2.1 Near and Far Detectors

One of the primary sources of systematic error is the uncertainty in the reactor neutrino flux. To minimize this uncertainty, near and far detectors, two identical detectors are needed. Each detector will contain 18.7m^3 of liquid scintillator target doped with 0.1% of gadolinium.

Figure 2.2 shows the layout of six reactors and two detectors and table 2.2 shows the neutrino flux contributions of reactors at each detector. The near and far detectors are placed $\sim 290\text{ m}$ and $\sim 1400\text{ m}$ away from the center of the reactors, respectively. The near detector is located under a 70 m (AMSL) ridge with an overburden of $\sim 110\text{ m}$ we whereas the far detector is located under a 260 m mountain with the overburden of $\sim 450\text{ m}$ we as shown in Figs. 2.2 and the coordinates of the detector center are measured with a total station to a precision of the order of 100 mm .

by weight?

add average thermal power of the reactor?

Reactor No.	Near Detector (%)	Far Detector (%)
1	7.06	14.24
2	15.54	16.31
3	33.80	17.82
4	26.71	18.28
5	11.37	17.53
6	5.52	15.83

Table 2.2: Fractional reactor neutrino contribution of reactor.

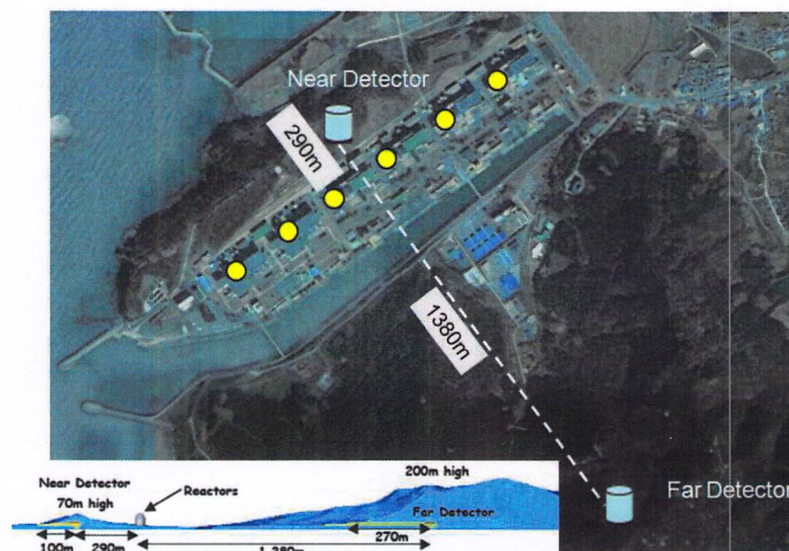


Figure 2.2: The yellow dots and light blue cylinder represent reactors and detectors, respectively. The six reactors are roughly equally spaced in a 1280 m span. The near and far detectors are 290 m and 1380 m away from the reactor array, respectively. The image taken from Google EarthTM and copyrighted there in. Bottom-left plot shows a side view.

✓

2.3 Detector Components

Both RENO near and far detectors consist of a cylindrical target of 140 cm in radius and 320 cm in height, providing a volume of 18.7 m^3 . Identical arrangement of the near and far detectors will significantly reduce the systematic errors of relative normalization to 0.6%. However, they will have different cosmic ray background levels because of unequal overburdens ($\sim 110 \text{ mwe}$ vs. $\sim 450 \text{ mwe}$). Although the near detector will suffer from higher cosmic ray background, it will observe much more signal events of reactor anti-neutrinos due to shorter distance from the nuclear cores and thus allows a high signal-to-background ratio.

→ on the neutrino flux?

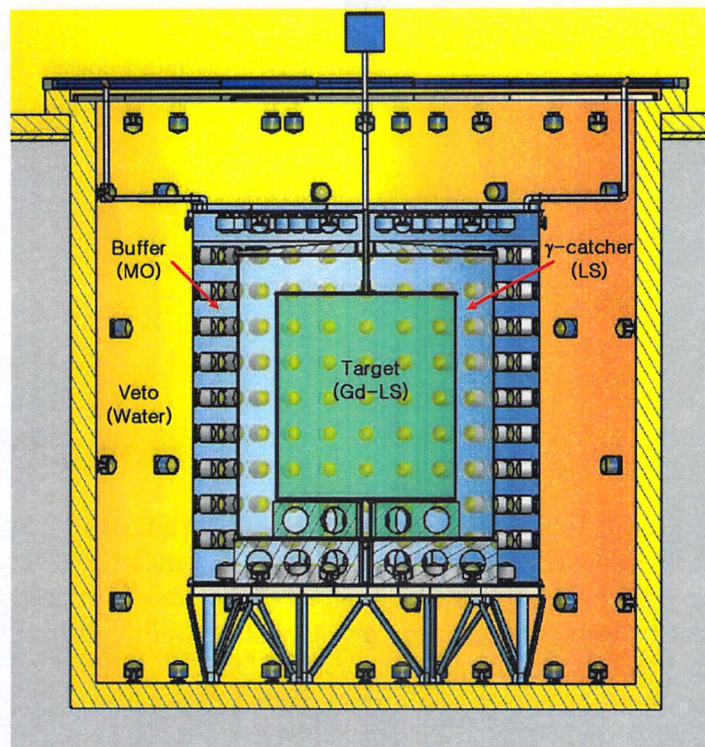


Figure 2.3: A schematic view of RENO detector. A neutrino target of 18.7 m^3 Linear Alkyl Benzene (LAB) based liquid scintillator doped with Gd is contained in a transparent acrylic vessel, and surrounded by 33.2 m^3 unloaded liquid scintillator of gamma catcher and 76.5 m^3 non-scintillating buffer. There are 354 and 67 10-inch PMTs mounted on buffer and veto vessel walls, respectively.

m^3

The RENO detector consists of a neutrino target, a gamma catcher, a buffer and a veto. Target and gamma catcher vessels will be made from acrylic plastic material, having transparency to the light of wavelengths above 400 nm. The acrylic vessels should hold aromatic liquids without leakage and its properties should not change for the duration of the experiment. They should not develop any chemical reaction with the scintillating liquids of neutrino target, gamma catcher and buffer for a long time period.

2.3.1 Target and Gamma Catcher

The two innermost layers, target and -catcher, are contained in vessels made of acrylic plastic. This acrylic plastic is transparent to photons with wavelengths above 400 nm. Two important issues for these layers are considered; chemical compatibility between the contents and the vessel, and mechanical stability.

As for the chemical compatibility, the liquid scintillating material for both the target and γ -catcher should not chemically interact with the vessel for the duration of the experiment. At the same time, the -catcher vessel should be chemically inert to the mineral oil in buffer layer. There have already been extensive studies on chemical compatibility of these materials for CHOOZ experiment and others. The RENO collaboration is also conducting various R&D on the chemical interaction of acrylic plastic and other materials used in the experiment.

Mechanically, these vessels are required to withstand the mechanical stresses that they are subjected to during the all phases of the experiment and maintain structural integrity. When loaded with liquids, the volume of the vessels can change slightly from the nominal volume. This change should be within specified tolerances.

2.3.2 Buffer

The buffer vessel is a cylinder of 5.8 m height and 5.4 m diameter containing target, γ -catcher, and buffer liquid. The buffer contains non-scintillating oil to shield the scintillating volume within from background sources outside, including radioactivity in PMTs. The bu_er vessel also acts as the PMT mounting surface where 354 PMTs are mounted staring inward and optically isolates the PMTs from the veto volume. The size of the bu_er vessel has been determined from the MC simulations.

2.3.3 Veto

The inner diameter and height of the veto vessel are 8.4 m and 8.8 m, respectively. The vessel is constructed with a 40 cm thick concrete vessel, as shown the outermost layer of Fig. 2.4. Inner surface of the concrete vessel was water-proofed with urethane resin. The water is purified at filling and continuously be circulated through a water purification system. There are 67 10-inch water-proof PMTs(R7081 Hamamatsu) attached on the inner surface of the veto vessel. The outer surface of buffer vessel and the inner surface of veto vessel is covered by Tyvek sheet to increase the light collection of Cherenkov photons in the water.

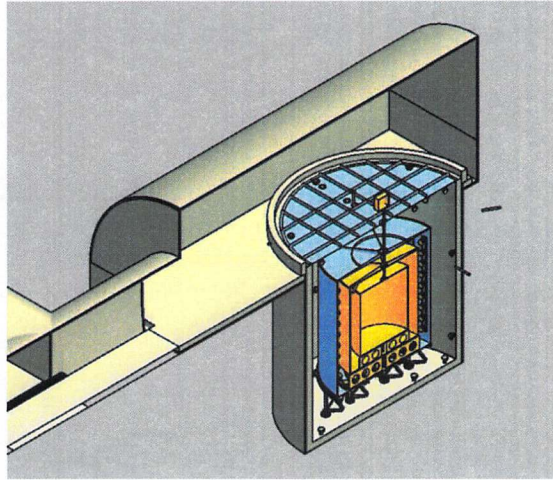


Figure 2.4: Cutaway view of RENO detector. The outermost region is veto and filled with filled water.

2.3.4 PMT

PMT Requirements and Specification

The scintillation lights from target and γ -catcher is detected with PMTs attached on the inner surface of the buffer vessel. The number of photoelectrons detected is estimated to be 150 photoelectrons per MeV for an event occurring at the center of the target. Since the minimum energy deposited in the detector by a positron emitted in the inverse beta decay process is 1.022 MeV, the average number of photoelectron per PMT in the buffer layer is ~ 0.5 . Therefore, the PMTs should be able to measure the single photoelectrons with high efficiency. The peak-to-valley ratio and the single photoelectron resolution of the PMTs are important parameters.

The main reason to isolate PMTs from γ -catcher via non-scintillating buffer region is to shield the γ -catcher from PMT's radioactivity. The radioactivity of PMTs needs to be studied to understand the rate of background originating from PMTs. The PMT background events are mainly in the low energy region of less than 2 MeV and could be misidentified as signals by accidental coincidence with neutron-like background events.

Since the PMTs is immersed in a layer of mineral oil, it is also important that the whole PMT assembly is chemically inert to mineral oil. The oil proofing should be stable for the duration of the experiment.

The quantum efficiency of each PMT is measured. We measured the quantum efficiencies of all PMTs with a relative accuracy less than 5%. The outlying PMTs was excluded from installation on the detectors.

~10-20 ms time scale

3. Data Selection

3.1 Production of $^{12}\text{B}/^{12}\text{N}$ in the RENO

^{12}B and ^{12}N radioactive isotopes can be generated by cosmic muons and they quickly undergo a beta decay process, emitting either an electron or a positron. In the RENO detector, these particles produce scintillating photons which can be converted to the energy by proper calibrations. We present the energy spectrum of the beta decay of the isotopes by analyzing the data collected by the RENO experiment.

Being similar with data selection criteria of muon-induced neutron, the method of coupling the prompt signal and delay signal was also applied. The difference here is that we used the prompt muon as the trigger event which could generate radioactive isotopes and the delay signal is the detection of electron or positron from decaying ^{12}B and ^{12}N .

3.2 Prompt Muon Signal Selection

3.2.1 Muon Energy Cut

Only cosmic ray muons can deposit energy larger than 20 MeV in our detector, the energy cut for prompt muon we set is 20 MeV.

3.3 Radioactive isotope candidate selection

3.3.1 Time Selection for Signal Time Window

Since the half-life of ^{12}B is 20.20 ms and the half-life of ^{12}N is 11 ms, we can set the upper limit of signal time window at three to four of their half-lives which is 60 ms. For the lower limit of signal time window, the main concern was to cancel the muon-induced spallation neutrons. We can easily find the significant 8 MeV n-Gd captured energy peak in the first 1 ms. Hence the low limit of signal time window was set at 1 ms to cancel these neutron events which might influence our time gap distribution and energy spectrum when doing data analysis.

3.3.2 Time Selection for Background Time Window

For the purpose of doing background subtraction to extract the energy spectra of ^{12}B and ^{12}N , the background time window was set from 200 ms to 200 s. After time selection cuts, the energy distributions of the candidate events are shown in Fig. 3.1.

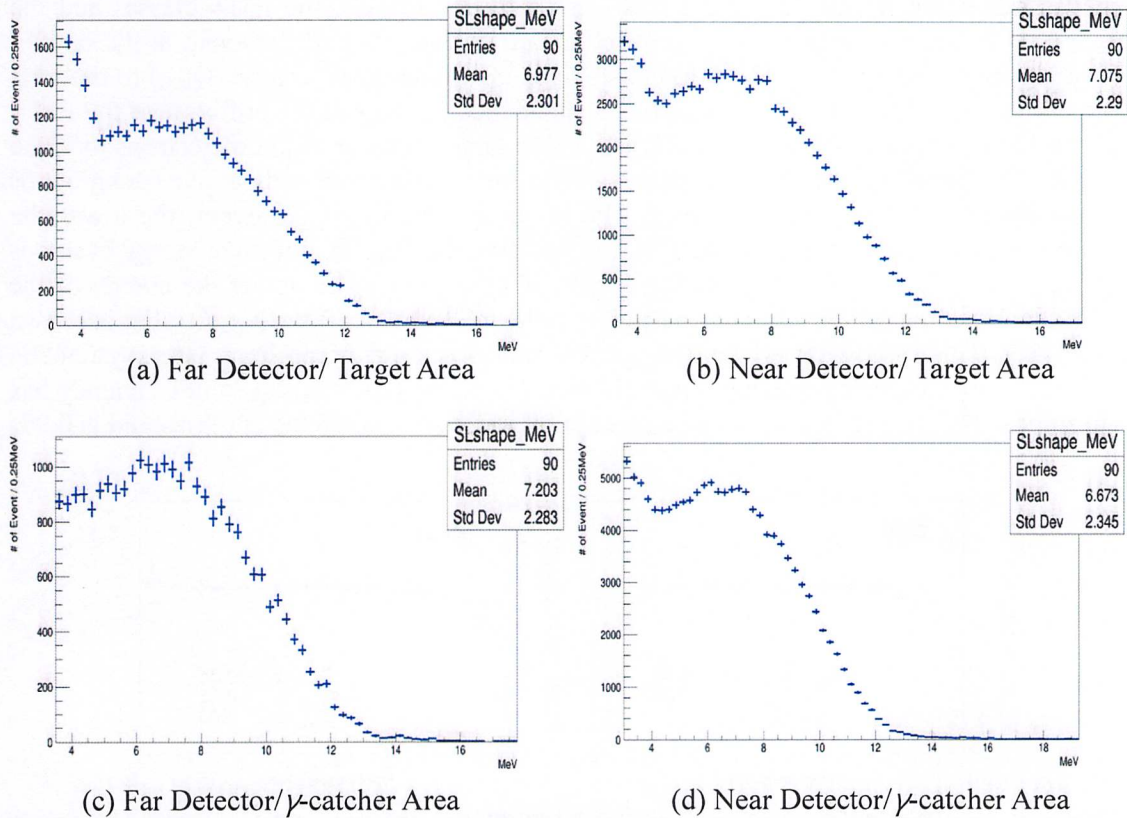


Figure 3.1: Energy spectrum of ^{12}B and ^{12}N candidates after applying the time selection cuts.

3.3.3 ^{12}B and ^{12}N Candidate Energy Cut

After considering all the correction both in theoretical and experimental prediction, the maximal energy of our delay signal that can be reached was still less than 16 MeV. The background with energy larger than the maximal value of our predicted energy may influence the time gap distribution, so we set the upper limit of ^{12}B and ^{12}N candidate energy cut at 16 MeV.

As shown in figure 3.1, for energy less than 3.5 MeV range we have large fluctuation due to large amount of lower energy background. The low limit of energy cut is set at 3.5 MeV to cancel these noises.

3.3.4 Vertex Cut

Since our detector only contains liquid scintillator in the 2800 mm-diameter vessel for the target and the 4000 mm-diameter vessel for the γ -catcher as shown in Table 2.1, this cut was set to ensure that our detector can capture all the decay energy deposited in our detector, which would influence the final energy spectrum and then affect our fitting result.

3.3.5 Flasher Cut

Energetic gamma rays and particles coming from the radioactive decay of isotopes in the inner detector can create accidental as well as correlated backgrounds. Some of these

for signal (60ms)

✓

✓

backgrounds come from surrounding rocks, the detector vessels, the PMT glasses and the mineral oil in the buffer, and can be reduced by using properties of the event at the border. These border events have a large ratio value of the maximum PMT charge (Q_{max}) to the total charge (Q_{tot}) (i.e. Q_{max}/Q_{tot}), because the events deposit energy at the buffer, near the PMT, and the PMT nearest to the events receives a much larger number of photoelectrons than the other PMTs. Therefore, the Q_{max}/Q_{tot} ratio is useful for reducing such radioactive backgrounds, but has an energy-dependent efficiency. The lower the energy of the event, the lower the number of photo-electron that hit the PMT. In addition the Q_{max}/Q_{tot} of high energy events is relatively larger than that of low energy events. In other words, the lower the energy of the event, the lower the efficiency. The energy dependent efficiency of the Q_{max}/Q_{tot} cut is shown in Fig. 3.3. This efficiency affects the spectra analyses, as it could be a large systematic uncertainty for measuring $|\Delta m_{ee}^2|$. To avoid this uncertainty, the Q_{max}/Q_{tot} cut efficiency has to be almost 100 %. Fig. 3.4 shows an almost 100% efficiency when the cut threshold is 0.07.

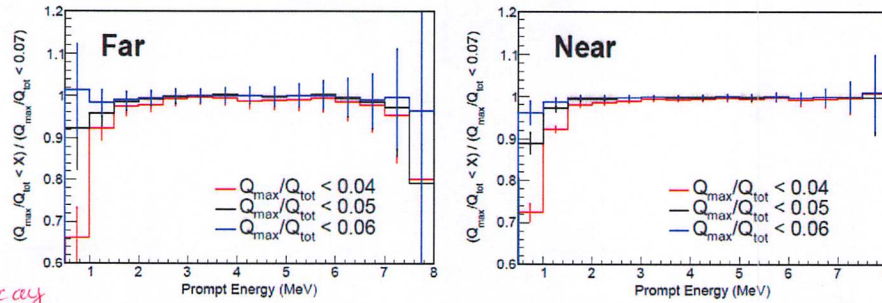


Figure 3.3: IBD Spectrum w.r.t the case in which the $Q_{max}/Q_{tot} < 0.07$ case. The left image shows the far detector and the right image shows the near detector. Under the assumption that the efficiency of $Q_{max}/Q_{tot} < 0.07$ is 100 %, this plot shows the Q_{max}/Q_{tot} cut efficiency has energy dependence.

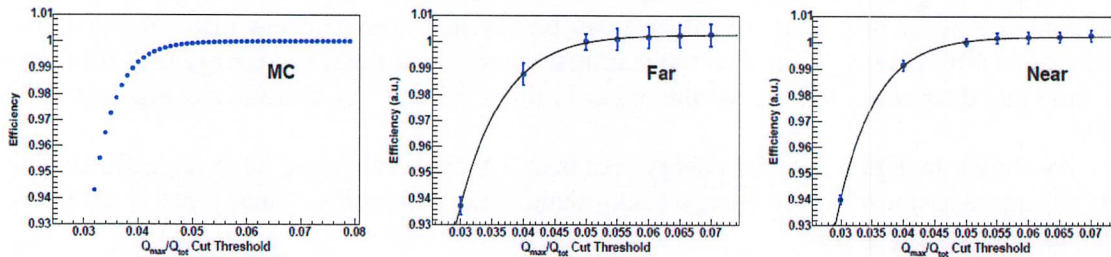


Figure 3.4: Q_{max}/Q_{tot} cut efficiency. The left image shows MC. The middle shows the far detector. The right image shows the near detector. The black line is the fitting result of a logistic function. The cut efficiency at 0.07 is $99.99 \pm 0.02\%$ at both detectors, according to the fitting results.

3.4 Data Set



There are two cases in which data analysis was changed from receiving data for 500 days from August 2011 to January 2013. One of them is ^{252}Cf Source Contamination at the end of 2012. The other one is DAQ Inefficiency due to UPS installation on January 20, 2013 at Near detector.

Since the near detector only considers 4 ~ 5% of DAQ efficiency, Data Set divides the period with the presence or absence of ^{252}Cf in the background. The reason for dividing the period by the presence or absence of Cf is to measure the Cf of the period in which Cf exists based on the period in which there is no ^{252}Cf .

Detector	Date	Run Number	Live Time[days]
Far	11 th Aug, 2011 ~ 21 th Jan, 2013	530 ~ 1748	489.9
Near	19 th Aug, 2011 ~ 21 th Jan, 2013	174 ~ 2321	458.4

Table 3.1 Data Set: Uses data before ^{252}Cf contamination among data of far and near detector.

3.5 Final selection criteria

- Prompt muon selection:
 1. Muon energy cut: energy > 20 MeV; 
- Delayed ^{12}B and ^{12}N candidate:
 1. Time selection for signal time window: (1 ms, 60 ms);
 2. Time selection for background time window: (200ms, 200s);
 3. ^{12}B and ^{12}N candidate energy cut : $3.5 \text{ MeV} < \text{Energy} < 16 \text{ MeV}$;
 4. Vertex cut: radius < 1400 (1970) mm and $|z| < 1600$ (2170) mm;
 5. Flasher cut: $Q_{\text{max}}/Q_{\text{tot}} = 0.07$;
 6. Trigger cut:
 - If there exists a muon (70MeV ~ 1.5GeV) in [-1ms, 0s] , reject the event
 - If there exists a muon (20 ~ 70 MeV , NHitVeto >50) in [-1ms, 0s], reject the event
 - If there exits any trigger in [-100us, 0], reject the event 

4. Monte-Carlo Simulation

4.1 Beta decay spectrum

Weak interaction is sufficient weak ⁱⁿ comparison with the interaction that forms quasi-stationary state, electromagnetic and strong interaction. So we take decay-causing interaction as weak perturbation. The transition rate is as follows, by Fermi Golden rule,

$$\lambda = \frac{2\pi}{\hbar} |V_{fi}|^2 \rho(E_f) \quad (4.1)$$

where V_{fi} is matrix element and $\rho(E_f)$ is density of states, $\rho(E_f) = \frac{dn}{dE_f}$ means the number dn of final states in the energy interval dE_f and $V_{fi} = \int \psi_f^* V \psi_i d\tau$. And Fermi expresses that operator V could be replaced with one of five mathematical operators O_x consistent with special relativity in his thesis. $X = V$ (vector), A (axial vector), S (scalar), P (pseudoscalar), or T (tensor). And in final states, there are an electron, neutrino, and daughter nucleus. So,

$$V_{fi} = g \int |\psi_f^* \phi_e^* \phi_\nu^*| O_x d\tau \quad (4.2)$$

where g is the constant that determines the strength of the interaction, ϕ_e^* , ϕ_ν^* is the eigenstate of electron and neutrino, respectively. $\rho(E_f)$ determines the shape of β energy spectrum. With momentum conservation of beta decay in CM frame, $\vec{p}_X' + \vec{p}_e + \vec{p}_\nu = 0$, number dn is expressed by

$$dn = dn_e dn_\nu = \frac{(4\pi)^2 p_e^2 dp_e p_\nu^2 dp_\nu V^2}{h^6} \quad (4.3a)$$

$$dn_{e,\nu} = \frac{4\pi p_{e,\nu}^2 dp_{e,\nu} V^2}{h^3} \quad (4.3b)$$

Suppose ϕ_e^* , ϕ_ν^* has usual free-particle eigenstate, normalized with the volume V to see only shape of β spectrum.

$$\phi_{e,\nu}^* = \frac{1}{\sqrt{V}} \exp(i\vec{p}_{e,\nu} \cdot \vec{r}) \quad (4.4)$$

If $T_e \approx 5\text{MeV}$, $p_e = 10.5\text{MeV}$, $\frac{p}{h} = 0.05\text{fm}^{-1}$, over nuclear volume, $\frac{p_e r}{h} \ll 1$,

$$\exp(i\vec{p}_{e,\nu} \cdot \frac{\vec{r}}{h}) = 1 + \frac{i\vec{p}_{e,\nu} \cdot \vec{r}}{h} + \dots \cong 1 \quad (4.5)$$

This approximation is called allowed approximation.

To obtain beta spectrum dependent only on p_e , partial decay rate for electrons is needed,

$$d\lambda(p_e) = \frac{2\pi}{h} g^2 |M_{fi}|^2 (4\pi)^2 \frac{p_e^2 dp_e p_\nu^2}{h^2} \frac{dp_\nu}{dE_f} \quad (4.6)$$

where $M_{fi} \equiv \int \psi_f^* O_x \psi_i d\tau$ is nuclear matrix element. Final state energy ignoring small recoil energy of daughter nucleus is $\frac{dp_\nu}{dE_f} = \frac{dp_\nu}{dE_\nu} = 1$ with E_e fixed. As far as the shape of the electron spectrum is concerned, the number of electrons with momentum between p_e and $p_e + dp_e$,

$$N(p_e) dp_e = C p_e^2 p_\nu^2 dp_e \quad (4.7)$$

In beta decay, electron also should be treated relativistically.

$$p_e^2 + m_e^2 = T_e^2 + 2m_e T_e + m_e^2$$

$$p_e = \sqrt{T_e^2 + 2m_e T_e}$$

$$dp_e = \frac{T_e + m_e}{\sqrt{T_e^2 + 2m_e T_e}} dT_e$$

With relativistic kinetic energy and energy conservation, $Q = T_e + p_e$,

$$N(T_e) dT_e = C \sqrt{T_e^2 + 2m_e T_e} (T_e + m_e) (Q - T_e)^2 dT_e \quad (4.8)$$

And correction for β 's Coulomb interaction with a daughter nucleus, the Fermi function, should be applied. So,

$$N(T_e) \propto \sqrt{T_e^2 + 2m_e T_e} (T_e + m_e) (Q - T_e)^2 F(Z_d, T_e) \quad (4.9)$$

where $F(Z_d, T_e)$ is Fermi function, Z_d is the atomic number of daughter nucleus.

4.2 Event generation for ^{12}B and ^{12}N β -decay

Event generation is the first step for MC simulation. Event generation includes generating beta's position in detector and momentum of beta. Vertexes should be generated uniformly in detector sized place because beta decay can be occurred anywhere in detector. And also produced beta has the beta energy spectrum in Section 4.2. We use TRandom3 class of ROOT program to generate random variable.

For the generation of uniform vertexes inside a Buffer sized cylindrical region, (x, y, z) are uniformly generated in rectangular box and then set of (x, y) are rejected if it is out of $\rho = \sqrt{x^2 + y^2}$. The result is shown in Figure 4.1.

And for the momentum of beta, we already know beta momentum, p following the beta spectrum Eq. 4.9 we need Cartesian coordinate

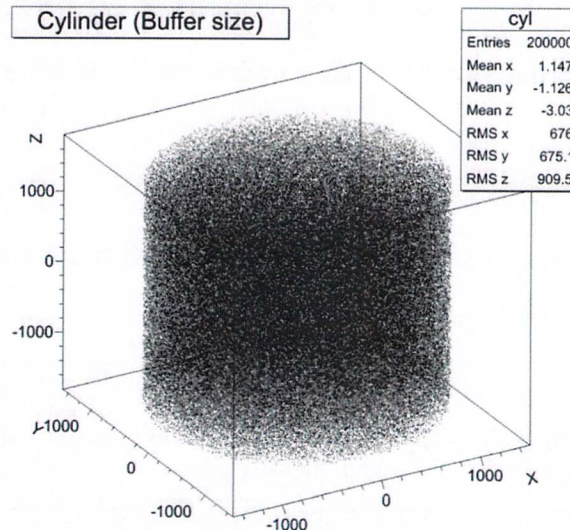


Figure 4.1: Random generation - Buffer size cylinder

component of momentum, p_x, p_y, p_z . So $p = \sqrt{p_x^2 + p_y^2 + p_z^2}$, momentum shell should be uniformly random generated. In spherical coordinate, $d\Omega = \sin\theta d\theta d\phi$, so we $u = \cos\theta$ to

satisfy $du = \sin\theta d\theta$, and then simply random generate u and \emptyset uniformly. Then we obtain Cartesian components of momentum that distributed uniformly in spherical coordinate as follows.

$$p_x = p\sqrt{1-u^2}\cos\emptyset \quad (4.10)$$

$$p_y = p\sqrt{1-u^2}\sin\emptyset \quad (4.11)$$

$$p_z = pu \quad (4.12)$$

Last, for beta energy spectrum, unstable QM state following the exponential decay has not definite but broad energy level. So the energy levels of decay-daughter are broad. The probability density of that energy eigenvalue is given as normalized Breit-Wigner formula. Breit-Wigner formula is driven.

Broad energy levels also give energy variations to the Q value of corresponding decay channel. And these energy variations follow the probability density, normalized Breit-Wigner formula. So it is applied as the variation of Q value in Eq. 4.9 with the probability of variation.

The final step is to simulate generated events using the RENO detector Monte Carlo (MC) simulation package. The same selection cuts are applied to simulated data for a comparison to data.

4.3 MC selection

- Nitrogen used only Dominant Branch Mode. In case of Boron, we use 3 branch modes which occupy 99%, and add up the following γ
- Using Uniform Distribution in Target and gamma-catcher Area
- Do not apply Q_{\max}/Q_{tot} Cut to MC
- Using the electron energy conversion function

The electron npe to MeV conversion function used in boron spectrum is different from the positron npe to MeV conversion function used in IBD events. We assume that the energy conversion functions are the same for the kinetic energy part and the only difference is 1.022MeV positron electron annihilation energy for the positron energy. Since data cannot distinguish between boron and nitrogen, the electron conversion function is applied to both nitrogen and boron.

5. Energy Calibration

RENO detector observe events (signal or background) collecting scintillation light via PMTs. First step is adjusting supplying high voltage value of PMT for the same gain values of each PMTs from one photo electron. This step make possible to convert pC to photo electron. Second step is converting photo electron to MeV from the several radioactive source data.

The energy response of the detector has varied with time. The detector needs to be monitored for response. So the calibration source run has been taking regularly. And delayed signal is used daily monitoring data and obtaining the daily charge correction factor.

5.1 Energy Calibration System

The detector cannot take regular run data which is used for IBD analysis during time that radioactive source data is in the detector. The event rate of source data is ~~too~~ higher than event rate of the regular run data. So the detector needs the source driving system. So that a 1D/3D source driving system were developed and is operated with custom computer software in the windows OS.

The 1D system was setting up for the target region. The wire is moving along the z-axis exactly the center of target vessel, the 1D system consists of a stepping motor, pulley and polyethylene wire. At the end of wire, the encapsulated source container is connected. At the end of the container, a weight made by teon is connected to counteracting buoyant force of liquid scintillator. The 1D system has an order of a few mm for the z-position accuracy that is much smaller than the vertex resolution (a few cm) of the detector. The design of 1D driving system is shown in Figure 5.1.

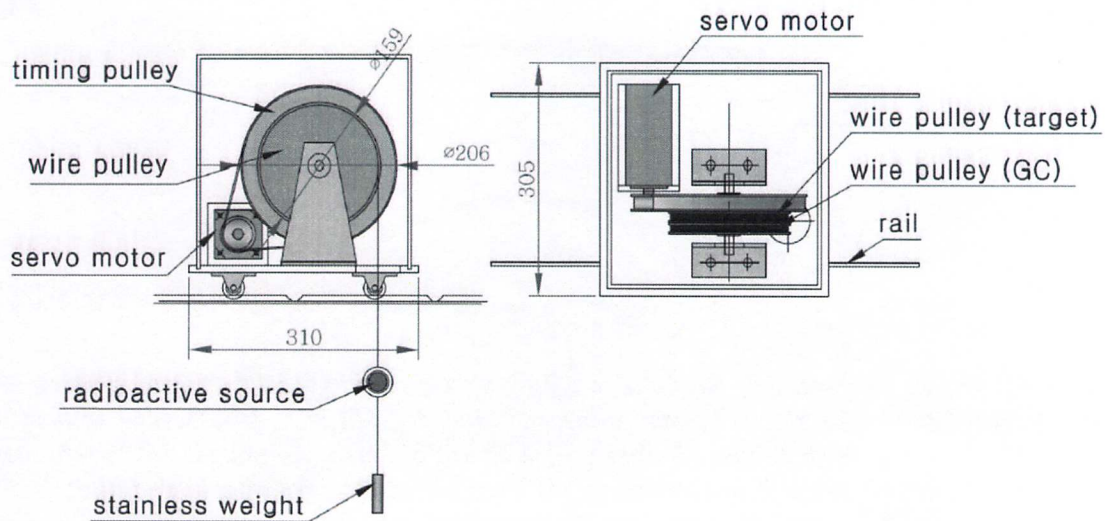


Figure 5.1: Design of 1D source driving system.

The 3D driving system can place the calibration source in the target region only. The system employs four rods to enable moving continuously the z direction of cylindrical coordinate. And uses a robot arm clinging to end of the rod to allow moving all θ direction and three ρ points of cylindrical coordinate as shown in Fig. 5.2. Figure 5.3 shows the 1D/3D calibration system installed at the detector.

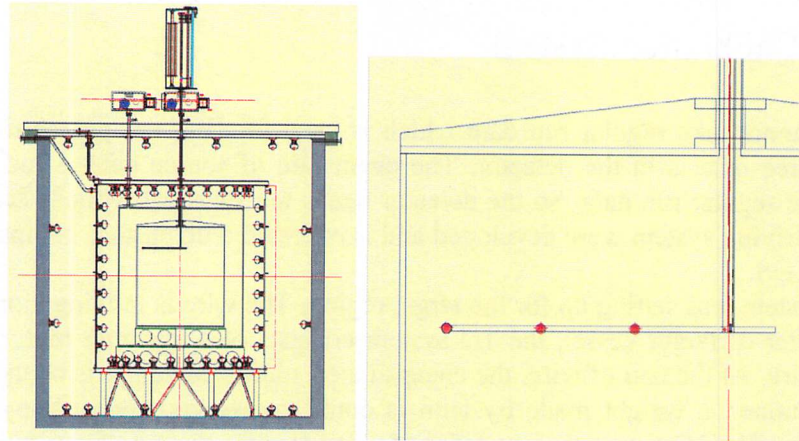


Figure 5.2: Design of 3D calibration system. The left plot shows cutaway view of 3D calibration system installing in the detector. The red dot in the right plots corresponds the position of the calibration source in the robot arm.



Figure 5.3: Installed 3D system. Two installed 1D system is also shown.

5.2 Energy Conversion Function

In the previous section, the source data and IBD candidates are well controlled for the time variation. From these corrected data, the p.e. values and corresponding MeV are known. So that p.e. to MeV conversion is possible from these data. Figure 5.4 shows the relation between p.e. and MeV of the each point. The n-H point is selected from the ^{252}Cf source data. The n-C point is added to obtain energy conversion function which is from ^{210}Po ^9Be source data. And the n-Gd point is from delayed signal of IBD candidates. Each point is converted to uniformly distributed positron event which is prompt signal of the IBD candidates from the center distributed source data except n-Gd point as following equation.

$$\text{P. E. / MeV} = \frac{\text{mean p.e. of source data} \cdot C_{\text{center-to-Uniform}} \cdot C_{\gamma\text{-to-}e^+}}{\text{MeV value of source data}} \quad (5.1)$$

where, mean p.e. of source data is from the charge corrected and additional corrected source data or charge corrected delayed of IBD candidates. $C_{center-to-uniform}$ is the values at the November 2012 that is reference date. And $C_{\gamma-to-e^+}$ is the correction factor for the conversion to positron to -ray from the source data. This correction factors are derived by comparing positron MC and source MC.

reference?
what is this value?

The energy conversion function is parameterized empirically using the following equation.

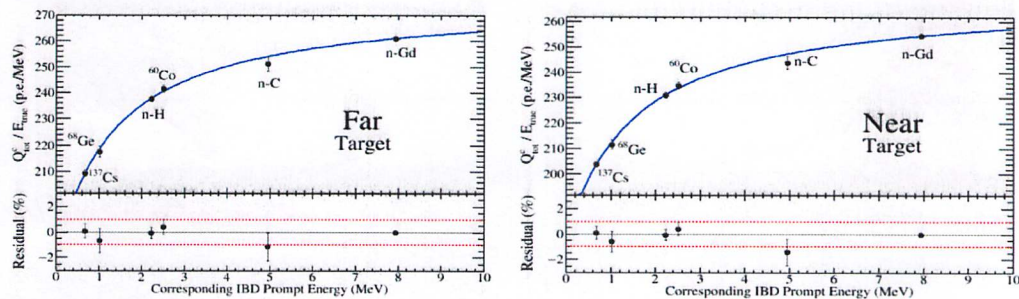
$$P.E./MeV = P_0 - \frac{P_1}{1 - \exp(-P_2 \cdot MeV - P_3)}$$

where P_0 , P_1 , P_2 , and P_3 are parameters determined from fitting to data. The fitting results are shown in Table 3.2 for target detector and gamma catcher detector separately and we use these parameters to measure the energy spectrum of the isotopes in each detector.

parameters \ Far Detector	Target	γ -catcher
P0	2.703293+02	5.035589e+04
P1	1.38801+-02	5.007947+04
P2	6.99516e-04	3.712670e+00
P3	5.13466e-04	4.270436e+00

parameters \ Near Detector	Target	γ -catcher
P0	2.63988e+02	2.990232e+02
P1	1.31526e-02	2.467878e+01
P2	6.17514e-04	1.493211e+00
P3	4.98241e-05	5.332941e-02

Table 3.2 Fitting parameters in the energy conversion function in target and gamma catcher respectively.



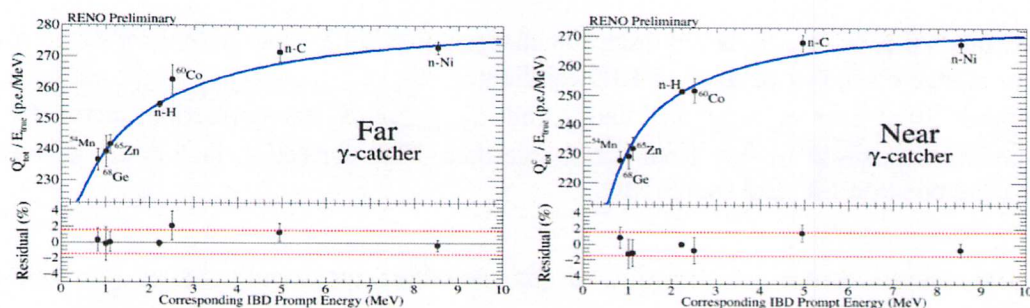


Figure 5.4: Energy conversion function. The top plot shows the near detector. And bottom plot shows the far detector. The point of n-H is from ^{252}Cf source data. The point of n-C is from $^{210}\text{Po}^9\text{Be}$ source data, and The point of n-Gd is from the delayed of IBD candidates.

6. Measurement of the energy spectrum of $^{12}\text{B}/^{12}\text{N}$ β decays

In this chapter, we extract the energy distributions of beta decays of ^{12}B and ^{12}N using fitting to muon time distribution and compare them with the Monte Carlo prediction.

6.1 Fitting Method to Measure $^{12}\text{B}/^{12}\text{N}$ Spectrum

Since boron and nitrogen isotopes are produced by cosmic muons, the time difference between the muon event and the isotope event show strong correlations as shown in Fig 6.1. Two components can be clearly observed in the figure. The short component is strongly correlated with the muon and is identified as $^{12}\text{B}/^{12}\text{N}$ component. The long component is not correlated or weakly correlated with muons and may include IBD events and other backgrounds.

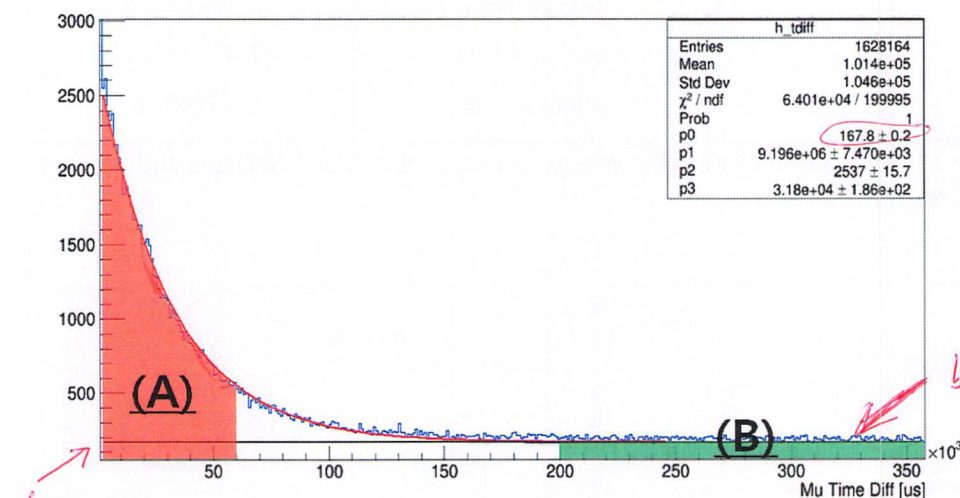


Fig 6.1 Muon Time Difference Distribution

explain a, b also in caption (not just in text)

blue line looks higher than 167?

Since the decay times of the isotopes are less than 20ms, the signal time window (region A) is set to be between 1ms and 60ms where the short component is dominant. The background time window (region B) is far from the signal time window and is set to be between 200ms and 200s. We expect that the contribution of the short component is negligible in the background time window. ✓

In the signal time window, the two components are mixed and we have to subtract the contribution of the long component in order to measure the energy spectrum of the isotopes. We assume that the energy distribution is not correlated with the muon time distribution for the long component. The energy distribution of the long component does not change whether a muon passes or not.

In order to estimate the contribution of the long component in the region A, we fit the muon time distribution using the two exponential functions each of which represents the short component and the long component respectively. Then we can estimate the scale factor α which is the ratio of the long component in the region A and the region B. From the region B, we can extract the energy distribution of the long component as shown in Fig 6.3 and by multiplying the distribution by the scale factor α , we can obtain the energy distribution of the long component in the signal time window. Then we subtract the scaled distribution from the energy distribution of the signal window (region A) (Fig 6.2) and get the energy distribution of the short component in the region A as shown in Fig 6.4. We apply this fitting method to measure the energy spectrum of $^{12}\text{B}/^{12}\text{N}$ in near target, near gamma catcher, far target, far and gamma catcher respectively. ✓

- Energy Spectrum(Short component) = Energy Spectrum(A) - $\alpha \times$ Energy Spectrum(B)
- Scale factor $\alpha = \frac{\text{Long component in (A)}}{\text{Long component in (B)}}$

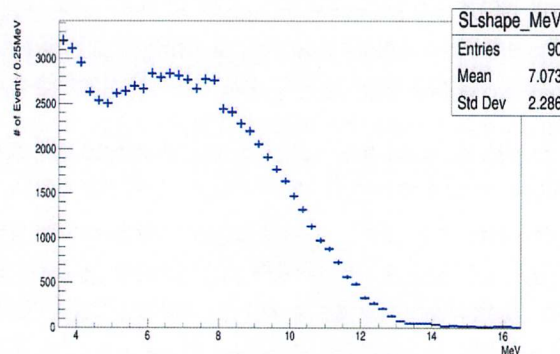


Fig 6.2 Energy Spectrum in the region A where $^{12}\text{B}/^{12}\text{N}$ and the background are mixed

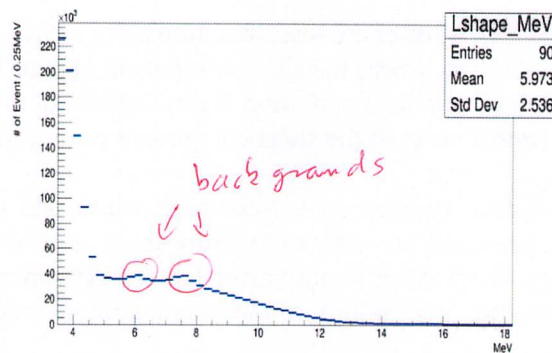


Fig 6.3 Energy Spectrum in the region B where the background is dominant

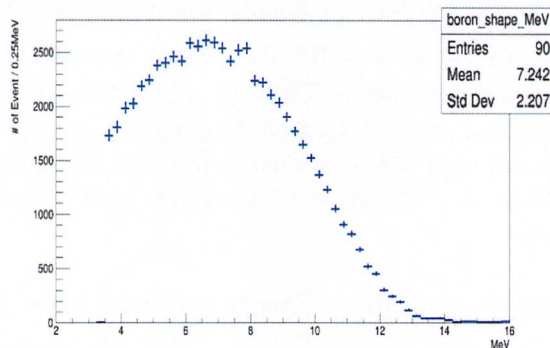


Fig 6.4 Energy Spectrum of the short component ($^{12}\text{B}/^{12}\text{N}$) in the region A

6.2 $^{12}\text{B}/^{12}\text{N}$ Energy Spectrum

Figures 6.5 (a), 6.6(a), 6.7(a), and 6.8(a) show the muon time difference distributions in far target, near target, far gamma catcher, and near gamma catcher detectors respectively. After applying the fitting method, we measure the energy distribution of $^{12}\text{B}/^{12}\text{N}$ as shown in figures 6.5(b), 6.6(b), 6.7(b) and 6.8(b) in far target, near target, far gamma catcher, and near gamma catcher detectors respectively.

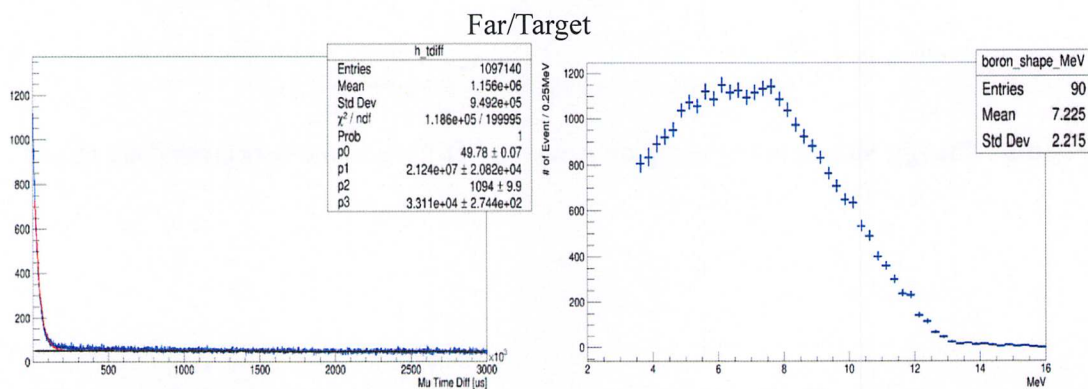


Fig 6.5 (a) Muon Time Difference

Fig 6.5 (b) $^{12}\text{B}/^{12}\text{N}$ Energy Spectrum

Near/Target

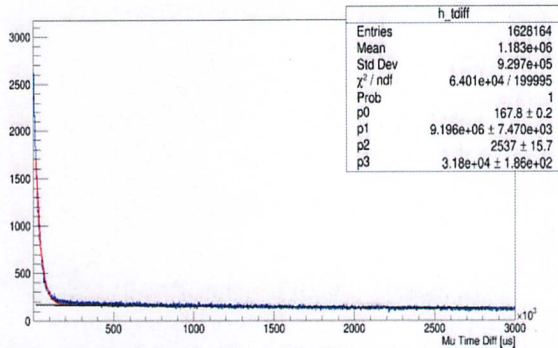


Fig 6.6 (a) Muon Time Difference Distribution

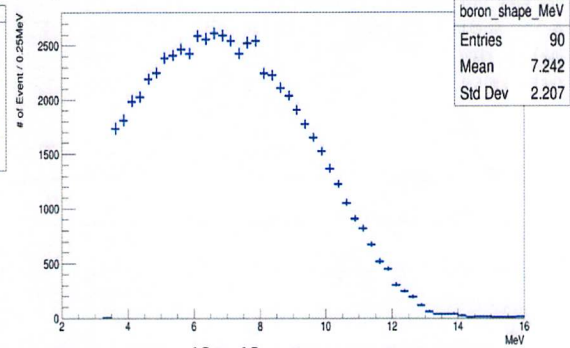


Fig 6.6 (b) $^{12}\text{B}/^{12}\text{N}$ Energy Spectrum

Far/ γ -catcher

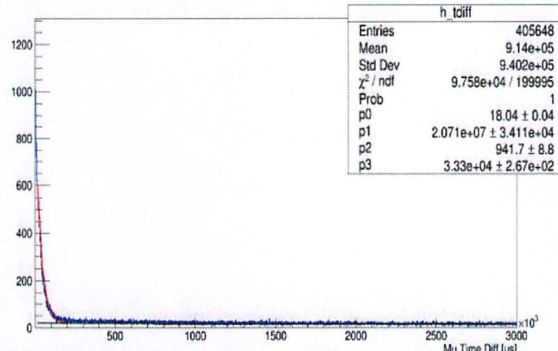


Fig 6.7 (a) Muon Time Difference Distribution

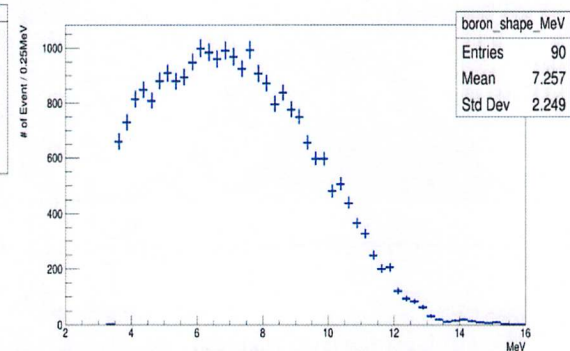


Fig 6.7 (b) $^{12}\text{B}/^{12}\text{N}$ Energy Spectrum

Near/ γ -catcher

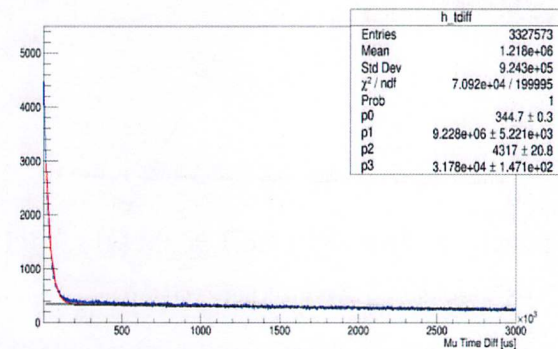


Fig 6.8 (a) Muon Time Difference Distribution

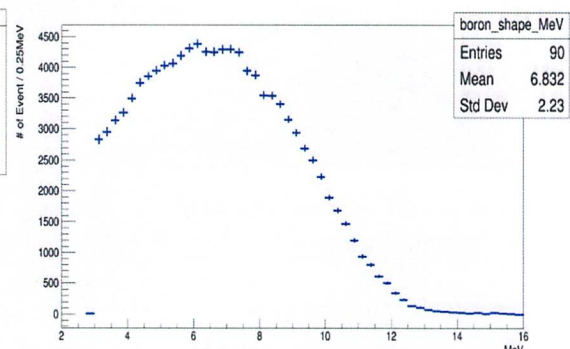


Fig 6.8 (b) $^{12}\text{B}/^{12}\text{N}$ Energy Spectrum

Figures 6.9, 6.10, 6.11, and 6.12 show the comparison between data and MC prediction. In general, the energy spectrum of $^{12}\text{B}/^{12}\text{N}$ shows good agreement with the MC distribution. However, in Fig 6.9 and Fig 6.10, some excess events over the MC prediction are observed around 8 MeV. We believe that this excess may come from neutron capture signals by Gd. Since the gamma catcher detector does not contain Gd, such excess may not be observed. In Fig 6.11 and Fig 6.12, we confirm that we do not observed any significant excess over the prediction.



Far/Target

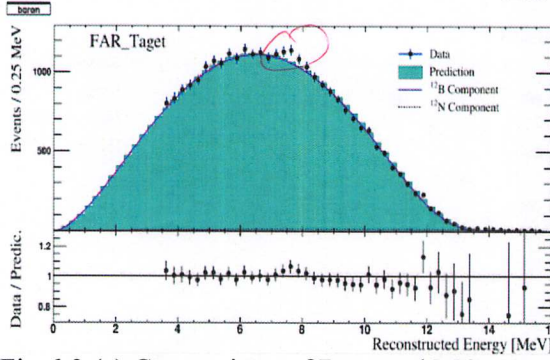


Fig 6.9 (a) Comparison of Data and MC

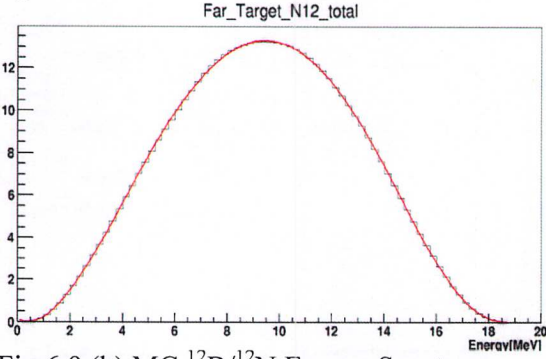
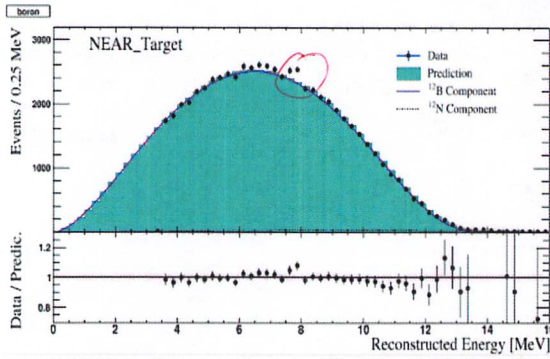


Fig 6.9 (b) MC $^{12}\text{B}/^{12}\text{N}$ Energy Spectrum

Near/Target



6.10 (a) Comparison of Data and MC

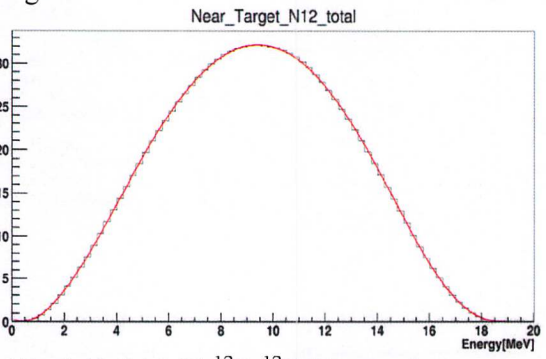
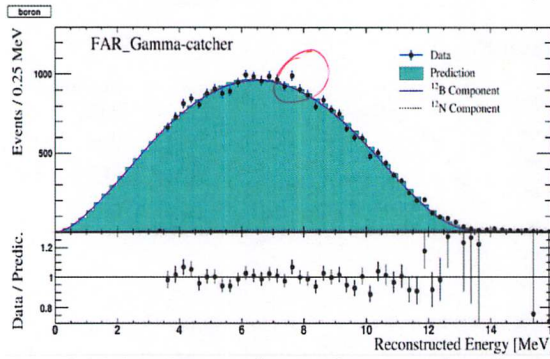


Fig 6.10 (b) MC $^{12}\text{B}/^{12}\text{N}$ Energy Spectrum

Far/ γ -catcher



6.11 (a) Comparison of Data and MC

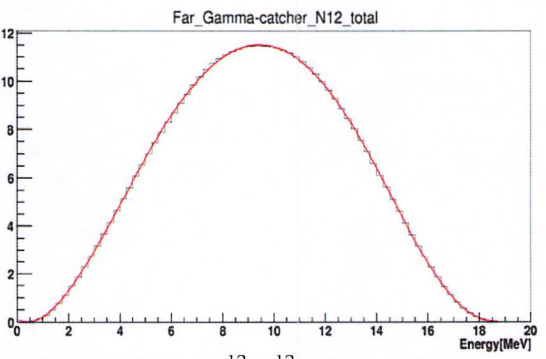
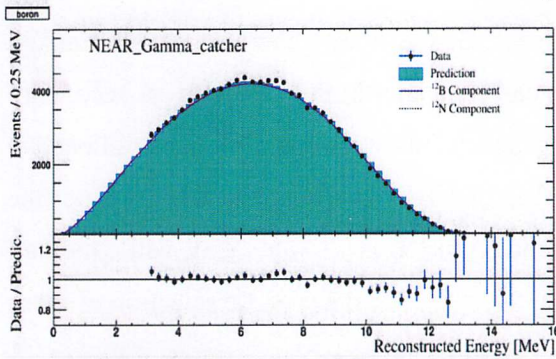


Fig 6.11 (b) MC $^{12}\text{B}/^{12}\text{N}$ Energy Spectrum

Near/ μ -catcher



6.12 (a) Comparison of Data and MC

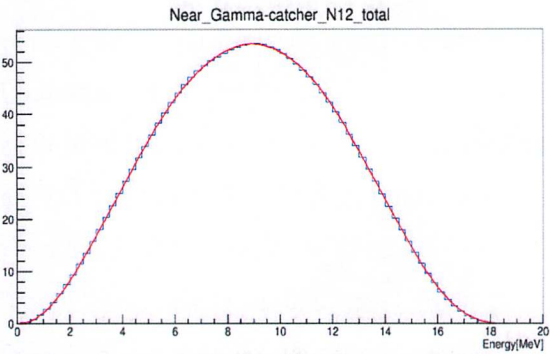


Fig 6.12 (b) MC $^{12}\text{B}/^{12}\text{N}$ Energy Spectrum

For consistency check, we also compare the energy distributions of the far detector and those of the near detector as shown in Fig. 6.13. They show very good agreement and confirm the concreteness of our result.

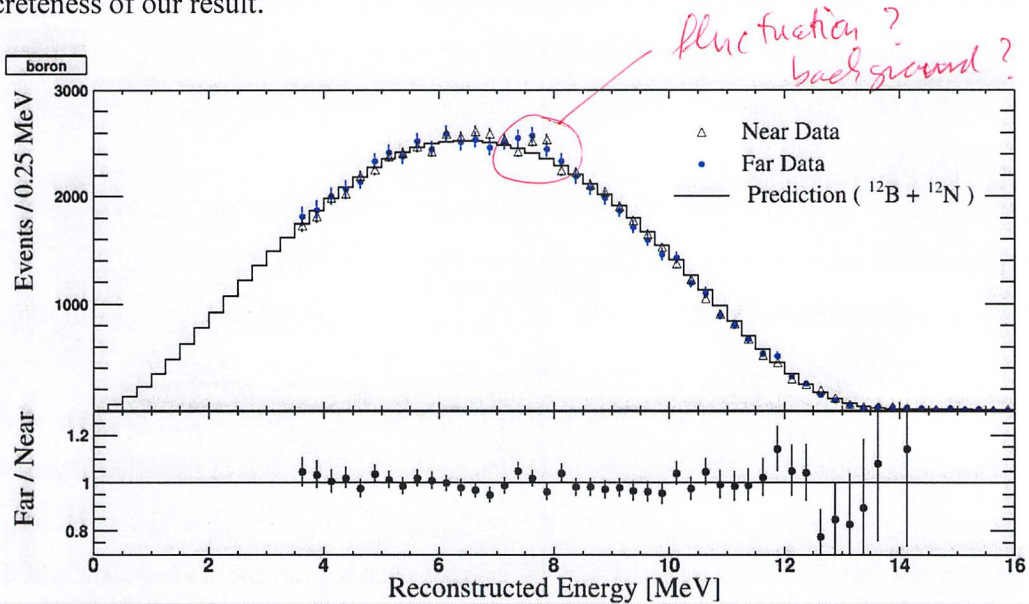


Fig 6.13 Comparison of the energy distributions in the near and the far detector

7. Summary

When muons from cosmic rays passing through the Gd-LS, they generate both Cherenkov and scintillation light. Muons being captured by carbon nuclei in the detectors, or secondary particles generated by muon spallation or electromagnetic showers could produce radioactive isotopes, which includes ^{12}B and ^{12}N . The half life of ^{12}B is 20.20ms and the Q value (the difference of energies of parent and daughter nuclides) of ^{12}B is 13.3689 MeV while the half life of ^{12}N is 11 ms and the Q value of ^{12}N is 17.3381 MeV. For the specific selection of those two isotopes, we set a time window from 1 ms to 60 ms which is about 3 times of their half-lives, and a energy cut from 3.5 MeV to 16 MeV. The 16 MeV upper limit of the energy cut makes the maximal Q value of those two isotopes involved into our selection range and the 3.5 MeV lower limits was to cut the low energy backgrounds. Vertex cut is to ensure that the detector can capture all the decay energy deposited in our detectors. For ruling out the flasher effects happen on PMTs inside our detectors, the same flasher cut is applied as the inverse-beta-decay analysis. ✓

The fitting methods, which includes a time domain fitting and an energy-time fitting, were used in the data analysis and have been tested with Monte Carlo simulation. In this study we use these method, which could use the time information and energy information detail in the same time and give us more reliable result. We measure the energy distributions of $^{12}\text{B}/^{12}\text{N}$ in the near and the far detectors using the energy conversion functions used in the inverse beta-decay analysis. We find that the energy spectra are in excellent agreement with the MC prediction, which shows the validity of the RENO energy calibration. ✓good! Furthermore we successfully reconstruct many isotope events from the RENO data and these distributions may be studied in detail to understand the underlying physics of the $^{12}\text{B}/^{12}\text{N}$ beta decays in the future. ✓

Part II

8. Production of Microscopic Black Holes

8.1 BLACK HOLES AT THE LHC

The primary goal of the LHC is to find the Higgs boson to confirm the standard model of particle physics. The other goal, which is equally important, is to search for signatures from new physics around 1 TeV. Low scale gravity models are subject to be tested by the LHC. The various quantum gravitational effects in particle interactions as well as the black hole formation are evident in these models. Currently, the LHC accumulates data with a high integrated luminosity and $\sqrt{s} = 7$ TeV collision energy in pp-frame. Before the scheduled shut-down at the end of 2012, the accumulated luminosity is expected to be more than 10fb^{-1} . At full power, the LHC is designed to produce luminosity greater than $10 - 100\text{fb}^{-1}$ per year with a center of collision energy of 14 TeV.

For the black hole, the basic observable quantity is the number of specific “black hole signals”, which can be expressed as:

$$N_{BH\text{ signal}} = \mathcal{L}_{LHC} \times \sigma(pp \rightarrow BH + X) \times Br(BH \rightarrow \text{signal}), \quad (8.1)$$

where \mathcal{L}_{LHC} is the luminosity of pp collision, which is accumulated by the LHC at a given time, $\sigma(pp \rightarrow BH + X)$ is the production cross-section for BH production and $Br(BH \rightarrow \text{signal})$ is the branching ratio of the decaying black hole to the signal.

The production cross-section of BH depends on the collision energy as previously discussed. The greater the collision energy is the larger the cross-section: $\sigma(E) \sim (G_D E)^{2/(D-3)}$ for semi-classical black holes. Thus, a higher energy runs with larger collision energy ($\sqrt{s} = 14\text{TeV}$) will have an obviously better chance of producing black holes than the current 7 TeV run. If possible, a future high energy collider with even higher CM energy, e.g., the VLHC with 100 TeV CM, is definitely more desirable. Giddings and Thomas (2001) and Dimopoulos and Landsberg (2001) estimated N_{BH} and concluded that the black hole production rate could be large, with $M_D \approx 1\text{TeV}$, but later developments also showed that there could be significant suppression of the rate. The most important factor is the threshold of black hole production. For a thermal or classical black hole, the energy threshold should be much larger than M_D or $\sqrt{s} \gg M_D$, otherwise quantum gravitational effects easily spoil the theoretical predictions. Based on the entropy counting, for instance, the threshold should be set to at $\frac{M_{min}}{M_D} > 5$ for semi-classical black holes. With this threshold, the cross-section is largely suppressed by PDF as shown by Cheung.

After a black hole is formed, it decays and emits Hawking radiation. The actual decay products depend on the number of extra dimensions, the mass, charge and angular momentum of the black hole, the wave function profile (the location) of particles in extra dimensions and also the geometry of the extra dimension. However, the large entropy of a black hole and the basic property of Hawking radiation determine some robust properties of the signature:

what
is G_D
 E, D

- Large multiplicity
- Flavor blindness

The large multiplicity of the signal is inherited from the large entropy of the thermal black hole. Thermal black holes typically have a large mass ($\gg M_D$) and the Hawking radiation contains large numbers of particles, jets, in particular. The flavor blindness of the black hole signal can be understood since the Hawking radiation is essentially thermal. Even when we take the greybody factors into account (which we will discuss later), flavor blindness remains. Statistically we would expect the same number of electron, muon and tau particles in the Hawking radiation. However, Hawking radiation depends on the spin of the particle and also on the number of degrees of freedom for each particle. For instance, a gluon has eight colorful degrees and the spin is one. An electron, on the other hand, does not carry any color charge and its spin is $1/2$ such that the portion in Hawking radiation is relatively smaller than a gluon.

8.1.1 Black hole production in particle collision

reference A black hole can be formed if energy is compressed into a sufficiently small volume. According to the Throne's hoop conjecture, a black hole can be produced when energy is concentrated in a spherical region with a hoop of proper circumference $2\pi R_s$. High energy particle collision can be one of the production mechanisms for a black hole formation when the impact parameter of incident particles is smaller than R_s .

From the hoop conjecture, the parton level cross section of a microscopic black hole is given as

$$\hat{\sigma} = r_s^2(\sqrt{\hat{s}}) \quad (8.2)$$

Here $r_s\sqrt{\hat{s}}$ is the radius of the D-dimensional Schwarzschild black hole with mass $\sqrt{\hat{s}}$. Calculations from numerical GR show black hole formation during the head-on collision of particles in 4D. Pretorius et. al showed a trapped surface can be formed by colliding particles. Two incident particles are modeled as classical spherical solitons with mass m_0 . They are set to travel toward each other with total energy of $E = 2\gamma m_0$ where γ is the relativistic Lorentz factor. Some portion of energy is spread out by gravitational wave. In general, particles collide with nonzero impact parameter b . Yoshino and Rychkov derived conditions to form apparent horizon (AH) from the collision of particles moving towards each other with the speed of light. The shape of apparent horizon is calculated numerically. They showed there is an upper bound of b to form a AH. Based on this, the hoop conjecture is modified by

$$\hat{\sigma}_{YR} = \pi b_{max}^2 \quad (8.3)$$

They also set the lower bound of the irreducible mass of a black hole by requiring its area to be one of apparent horizon, A_H . Therefore,

$$M_{irr} \geq M_{AH} = \frac{(D-2)\Omega_{D-2}}{16\pi G_D} \left(\frac{A_H}{\Omega_{D-2}}\right)^{(D-3)/(D-2)} \quad (8.4)$$

Since the area of a black hole never decreases classically, the minimum area of rotating black hole is set to the area of Schwarzschild black hole with its mass, M_{irr} . This condition is reduced to the bounds on the initial black hole mass and angular momentum,

why irr?
meaning?

$$M_b(J) = M_{AH} \left\{ 1 + \left[\frac{(D-2)J}{2M_{AH}} \right]^2 \left[\frac{(D-2)\Omega_{D-2}}{16\pi G_D M_{AH}} \right]^{2/(D-3)} \right\}^{1/(D-2)} \quad (8.5)$$

At the first stage of the black hole formation from particle collision, it is believed that a chunk of energy is formed within a volume. Gravitational waves are generated from the collision event and some portion of energy and angular momentum will be lost. But there is upper bound on the energy loss, at least M_{irr} will remain to form a rotating black hole. Angular momentum will be lost in the same way within the allowed range of angular momentum in the Equation 8.5. This phase is often called as balding phase.

8.1.2 The production cross section in a pp collision

The LHC is a proton-proton (pp) collision machine. Each proton is composed of several partons, and each parton carries a part of the proton energy and interacts with other partons or passes by as a spectator at the moment of collision. The actual collision energy therefore is less than the total energy of protons, but a part of it. Fig. 8.1 is a schematic of pp collision that produces a black hole of mass $\sqrt{x_1 x_2 s}$ and angular momentum J . Considering the parton distribution function (PDF), and the $f_i(x, Q^2)$ of each parton (i), the hadron level cross-section is obtained as:

$$\sigma_{pp \rightarrow BH+X} = \int_{M_{D^2/s}}^1 du \int_u^1 \frac{dv}{v} \sum_{ij} f_i(v, \hat{s}) f_j\left(\frac{u}{v}, \hat{s}\right) \hat{\sigma}_{ij \rightarrow BH}, \quad (8.6)$$

where, $\hat{\sigma}_{ij \rightarrow BH}$ is the cross-section of the two partons (i and j). The sum runs $i, j = (q, \bar{q}, q)$ and $q = (u, d, s, c, b)$, i.e., partons in a proton.

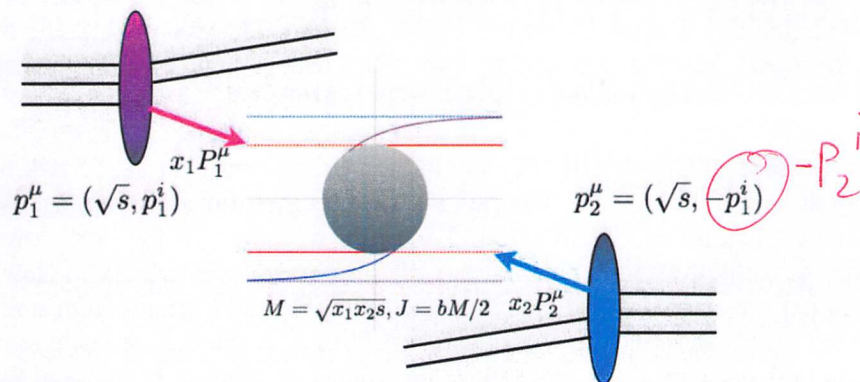


FIG. 8.1 A schematic view of black hole formation in pp collision.

8.1.3 Black hole decay by Hawking radiation

In the first stage of production, the concentrated energy is not settled down to a simple, symmetric black hole, but rather violently emitting gravitational waves. This stage is called the balding phase after the ‘no-hair’ theorem. The *spin-down phase* follows after the balding phase. In the spin-down phase, the black hole is well described by the MP solution with one rotation parameter. In this stage, Hawking radiation takes energy and angular momentum away so that the rotation of the black hole slows down and proceeds to the non-rotating phase or the Schwarzschild phase. In the Schwarzschild phase, the rest of the energy is emitted as Hawking radiation, which is rather symmetric and democratic (equal for each species). At the end of the Schwarzschild phase, the mass of the black hole becomes not much greater than M_D for which a full quantum gravitational description is required. We schematically illustrate the evolution of the black hole produced in particle collision in Fig. 8.2 including the balding, spin-down, Schwarzschild and the final Planck phase where $M \sim M_D$.

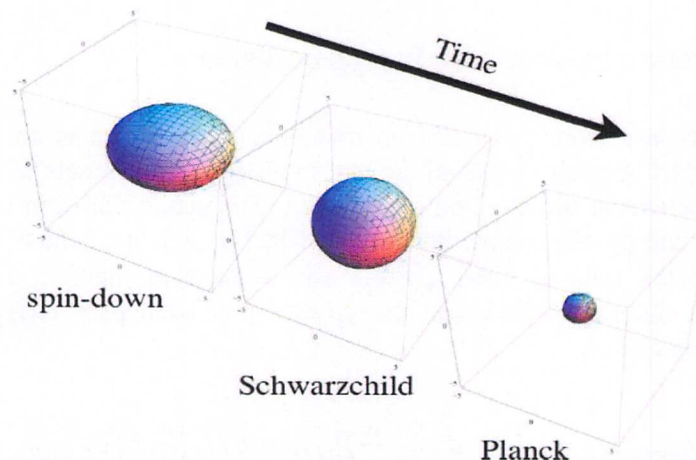


FIG. 8.2 Evolution of black hole via Hawking radiation. The geometry becomes more spherically symmetric in spin-down phase. When the angular momentum is lost completely, Schwarzschild phase takes over then black hole evolves toward the Planck phase.

9. CHARYBDIS II Monte-Carlo simulation

9.1 CHARYBDIS II: A Black Hole Event Generator

We present results of CHARYBDIS2, a new Monte Carlo simulation of black hole production and decay at hadron colliders in theories with large extra dimensions and TeV-scale gravity. The main new feature of CHARYBDIS2 is a full treatment of the spin-down phase of the decay process using the angular and energy distributions of the associated Hawking radiation. Also included are improved modeling of the loss of angular momentum and energy in the production process as well as a wider range of options for the Planck-scale termination of the decay. The new features allow us to study the effects of black hole spin and the feasibility of its observation in such theories.

9.2 Incorporation of the results into CHARYBDIS2

9.2.1 BLACK HOLE PRODUCTION CROSS SECTION

In earlier versions of CHARYBDIS, parton-level cross sections for different D values were calculated according to the simple formula $\sigma = \pi r_s^2(\sqrt{s})$ which is based on Thorne's hoop conjecture. Here $r_s(\sqrt{s})$ is the radius of the D -dimensional Schwarzschild black hole with mass \sqrt{s} . Incorporation of the Yoshino-Rychkov cross section results simply requires multiplying these σ values by the 'formation factors'. The increase in σ ranges from a factor of 1.5 at $D = 5$ to 3.2 at $D = 11$. The maximum impact parameters for black hole production, b_{max} , to be generated in CHARYBDIS2, is adjusted accordingly (the two are related through $\sigma = \pi b_{max}^2$).

The parton level cross section is conveniently parameterized by C -factors as $\hat{\sigma}_{ij} = C_{ij}\hat{\sigma}_0$ where $\hat{\sigma}_0 \approx F\pi_{sch}^2 = F\frac{2\sqrt{s}}{3T^3}$ is the conventional cross section. ✓

9.2.2 5D wave functions

As shown in Eq. 1, the 5D coordinate is given in an interval $y = [0, L]$. We set the gauge bosons have at wave function profile. The 5D gauge field can be decomposed as

$$A_\mu(x, y) = \sum_{n=0}^{\infty} A_\mu^{(n)}(x) \chi_A^{(n)}(y), \quad \chi_A^{(0)} = \frac{1}{\sqrt{L}} \quad (9.1)$$

where $\chi_A^{(n)}$ the 5D wave function and n is describe each KK modes. Since the fermion wave function profiles is not at, the 5D wave function is non-trivial. Considering the Dirac fermion with mass m in the bulk, we can derive the 5D wave function profiles.

$$\begin{aligned} \Psi_{L,R}(x, y) &= \sum_{n=0}^{\infty} \psi_{L,R}^{(n)}(x) e^{\frac{3}{2}\sigma} \chi_{L,R}^{(n)}(y), \\ \chi_{L,R}^{(0)} &= N_{L,R}^{(0)}(\nu) \frac{e^{\left(\frac{1}{2} \pm \nu\right)\sigma}}{\sqrt{L}} \end{aligned} \quad (9.2)$$

where $\nu = m/k$ the normalization coefficient $N_{L,R}^{(0)}(\nu) = \sqrt{\frac{kr_c(1 \pm 2\nu)}{e^{kr_c\pi(1 \pm 2\nu)} - 1}}$. The fermion wave function profile is determined by ν . These 5D wave functions χ satisfy the following normalization condition

$$\int_0^L dy \chi^{(n)}(y) \chi^{(m)}(y) = \delta_{nm} \quad (9.3)$$

9.2.3 Cross section

The parton level cross section of black hole which produced in the bulk at position y is given by

$$\begin{aligned}\hat{\sigma}_{BH}(y) &= \pi r_{sch}^2(\sqrt{s}) = \frac{2}{3} \left(\frac{\sqrt{s}}{M_5} \right)_{IR} \frac{1}{M_5^2(y)} \\ &= \frac{2}{3} \left(\frac{\sqrt{s}}{M_5} \right)_{IR} \frac{e^{2k(y-L)}}{M_5^2(L)} \\ &= \hat{\sigma}_0 e^{2k(y-L)}\end{aligned}\tag{9.4}$$

where $\hat{\sigma}_0 = \frac{2}{3} \left(\frac{\sqrt{s}}{M_5} \right)_{IR}$ is the (conventional) cross section defined on IR. In our set up, the gravity scale is position dependently determined as $M_5(y) = e^{-ky} M_5(0)$. The dimensionless ratio \sqrt{s}/M_5 , however, is scaling independent thus y independent. Eventually we get $\hat{\sigma}_{BH}(y) \propto e^{2k(y-L)}$, which is exponentially peaked at $y = L$. The effective parton level cross section in 4D is obtained after integrating over the 5th dimensional coordinate y .

$$\begin{aligned}\hat{\sigma}_{BH,ij}^{eff} &= \int_0^L dy \hat{\sigma}_{BH}(y) \chi_i(y) \chi_j(y) \\ &= \sigma_0 \int_0^L dy e^{2k(y-L)} \chi_i(y) \chi_j(y) \\ &\equiv \sigma_0 C_{ij}\end{aligned}\tag{9.5}$$

where χ_i is wave function profile for parton and i, j indicate the species of parton. The coefficient C_{ij} which we will call C – factor gives the relative suppression due to the profile of each parton.

9.2.4 C – factors

The black hole can be produced in three different parton combination gluon-gluon, gluon-quark and quark-quark. We can get analytic form of the C -factors using the 5D profiles Eq. 9.6-9.7 and the black hole production cross section formula Eq.9.5 .

We set the gauge bosons have at wave function profile. The 5D gauge field can be decomposed as

$$A_\mu(x, y) = \sum_{n=0}^{\infty} A_\mu^{(n)}(x) \chi_A^{(n)}(y), \quad \chi_A^{(0)} = \frac{1}{\sqrt{L}}\tag{9.6}$$

where $\chi_A^{(n)}$ is the 5D wave function and n describe each KK modes. Since the fermion wave function profiles is not at, the 5D wave function is non-trivial. Considering the Dirac fermion with mass m in the bulk, we can derive the 5D wave function profiles.

$$\Psi_{L,R}(x, y) = \sum_{n=0}^{\infty} \psi_{L,R}^{(n)}(x) e^{\frac{3}{2}\sigma} \chi_{L,R}^{(n)}(y),$$

$$\chi_{L,R}^{(0)} = N_{L,R}^{(0)}(v) \frac{e^{\frac{1}{2}(\pm v)\sigma}}{\sqrt{L}} \quad (9.7)$$

- $gg \rightarrow BH$

$$C_{gg} = \int_0^L \frac{dy}{L} e^{2k(y-L)} = \frac{1-c}{2kL} \approx \frac{1}{2kL} \approx \frac{1}{71} \quad (9.8)$$

- $f_{L,R} f'_{L,R} \rightarrow BH$

$C_{f,f'}$

$$\begin{aligned} &= \int_0^L \frac{dy}{L} N_f^{(0)}(v_1) N_{f'}^{(0)}(v_2) e^{\sigma} e^{2k(y-L)} e^{(\pm v_1 \pm v_2)\sigma} \\ &= \frac{\sqrt{(1 \pm 2v_1)(1 \pm 2v_2)}}{3 \pm \pm v_1 \pm v_2} \frac{e^{kL(1 \pm v_1 \pm v_2)} - e^{-2kL}}{\sqrt{(e^{kL(1 \pm 2v_1)} - 1)(e^{kL(1 \pm 2v_2)} - 1)}} \end{aligned} \quad (9.9)$$

- $gf_{L,R} \rightarrow BH$

$$\begin{aligned} C_{gf_{L,R}} &= \int_0^L \frac{dy}{L} N_f^{(0)}(v) e^{\frac{\sigma}{2}} e^{2k(y-L)} e^{\pm v\sigma} \\ &= \frac{1}{\sqrt{kL}} \frac{\sqrt{1 \pm 2v}}{\pm v + 5/2} \frac{e^{kL(\pm v + 1/2)} - e^{-2kL}}{\sqrt{e^{kL(1 \pm 2v)} - 1}} \end{aligned} \quad (9.10)$$

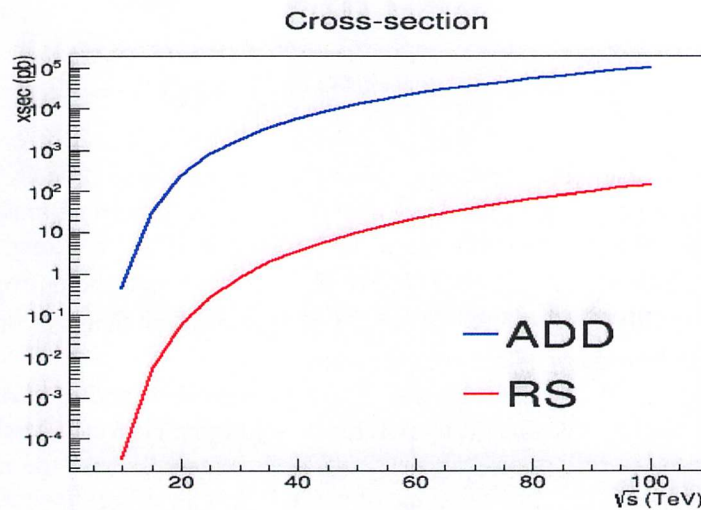


FIG. 9.1. Production cross section vs. center of mass energy

10. Study of microscopic black holes in 100TeV p - p collisions

10.1 Black hole in the Randall-Sundrum model and ADD model

The Randall-Sundrum model is yet another theoretical model with a Large Extra Dimension where the extra dimension has curved geometry. This 5 dimensional theory of course has explanation on the hierarchy problem of the Plank scale to the Electroweak scale, but can also give answers for the Yukawa hierarchy problem of fermions.

As in the ADD model, the detection of black holes is a very effective way to prove the RS model. We will review the RS model and properties of RS black holes in this chapter to see difference of black hole's behavior in RS model compared to the ADD black hole.

10.2 ADD black hole and RS black hole

If a black hole is small enough (i.e., $r_h \ll r_c$) the small black hole can be regarded as a higher dimensional black hole with s^{2+n} event horizon topology in $4 + n$ dimensions. As long as the curvature radius is large compared to the size of the event horizon, there seems to be no qualitative

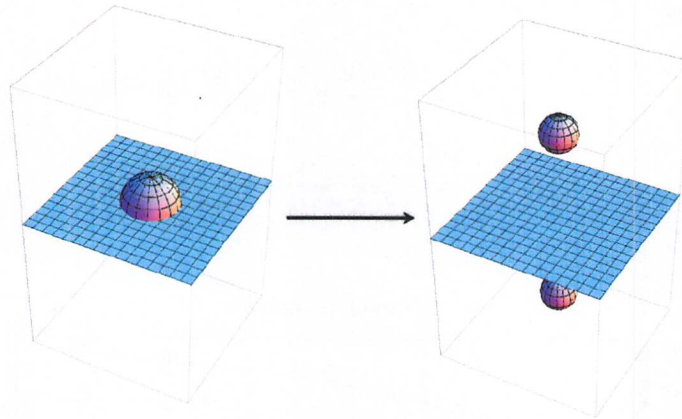


FIG. 10.1. A black hole on the brane recoils with bulk radiation. This process is forbidden in the presence of \mathbb{Z}_2 symmetry about the brane position. A black hole of mass M should be split into two smaller black holes with mass $M/2$ for each if \mathbb{Z}_2 is exact. However, the entropy of the initial black hole is $S_{ini} = S(M) \propto M^{(2+n)/(1+n)}$ and the entropy for the final black holes is $S_{final} = 2S(M/2) \propto 2M^{(2+n)/(1+n)} < S_{ini}$, smaller than the original entropy. Thus, such a process is forbidden by the area theorem.

Distinction between a black hole in the ADD background and the one in the RS background; both are well approximated by MP black solutions. However, it should be noted that RS geometry has a \mathbb{Z}_2 reflection symmetry about the 'brane' where the mini black hole is likely to be produced such that the behavior of a black hole in different scenarios might be distinguishable. An ADD black hole radiates mostly to the bulk in the first phase of production, particularly due to the large angular momentum. A black hole can recoil and leave the brane. However, for a RS black hole, bulk radiation is strongly suppressed due to

the small number of bulk degrees of freedom and the presence of \mathbb{Z}_2 symmetry. A black hole cannot recoil and leave the brane. ✓

10.3 100 TeV colliders' safety in the context of stable micro black holes production

In the theories with extra dimensions the higher-dimensional Planck mass could be as small as 1 TeV, which entails the possibility that a considerable amount of microscopic black holes can be produced during runs of future high energy colliders. We calculate the cross sections of the black hole production at the 100 TeV collider in previous chapter, the fraction of the black holes trapped inside the Earth and the resulting rate of production. ✓

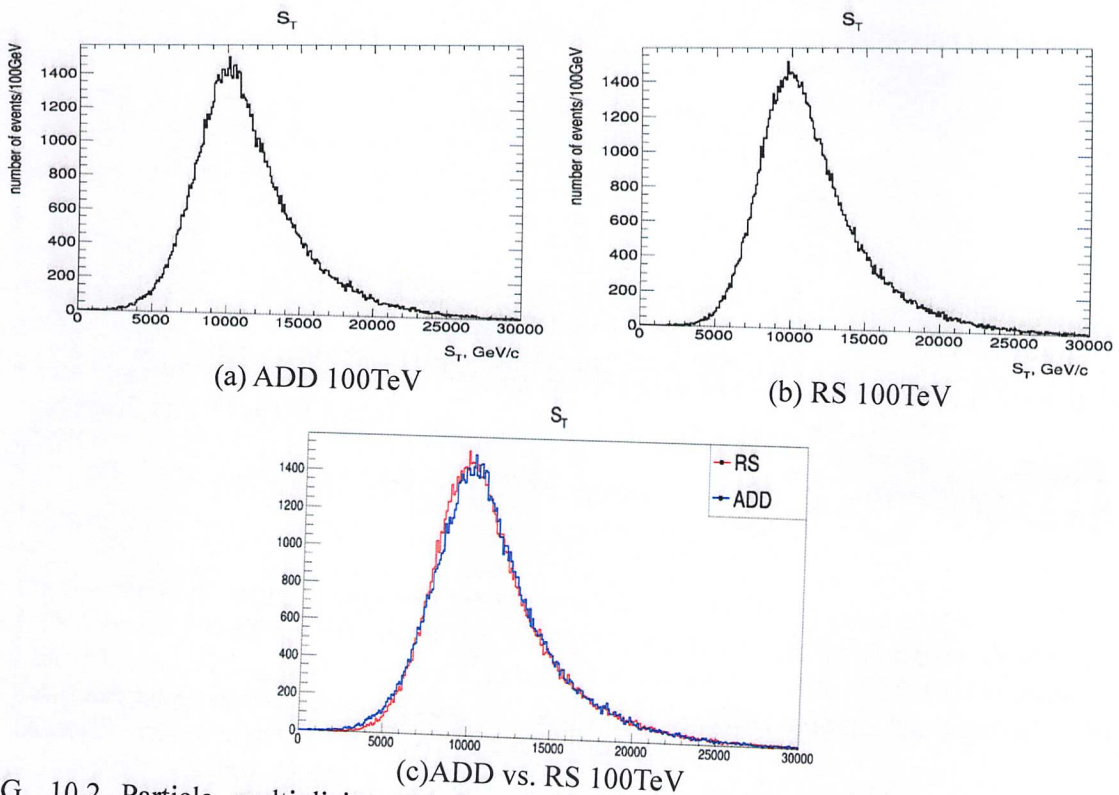
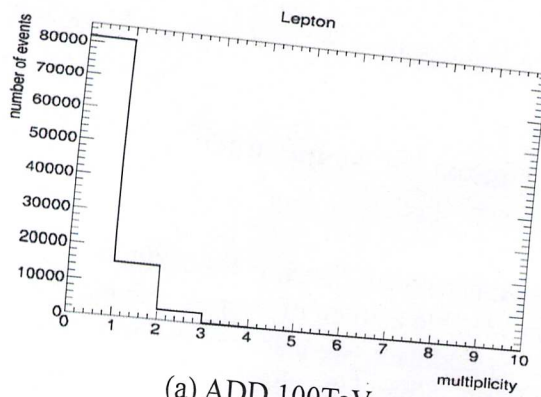
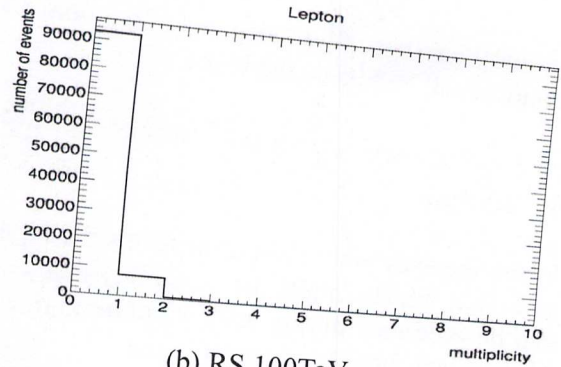


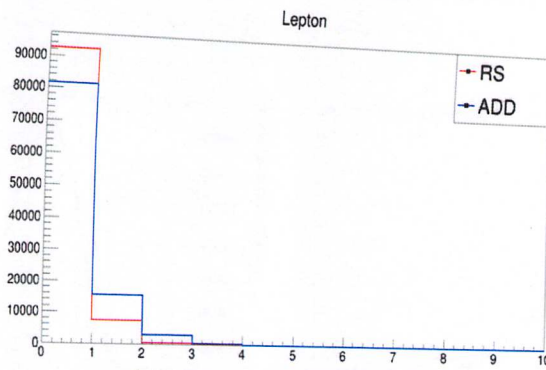
FIG. 10.2 Particle multiplicity and S_T . S_T variable is defined as sum of transverse momentum of particles.



(a) ADD 100TeV

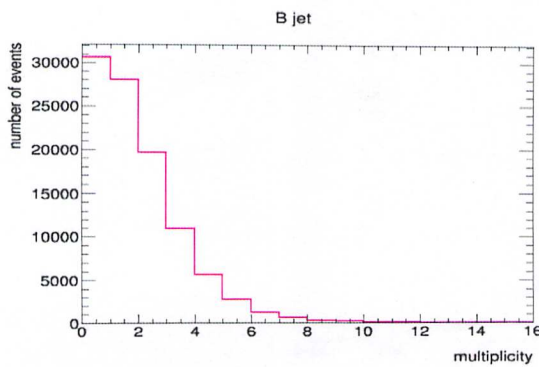


(b) RS 100TeV

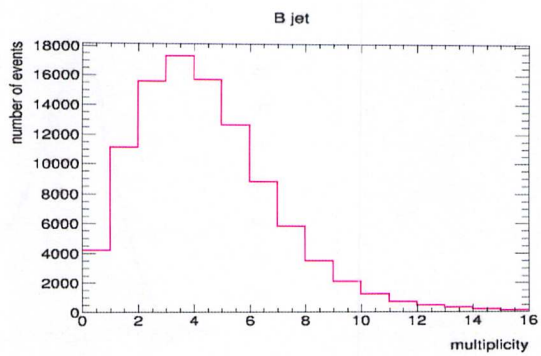


(c) ADD vs. RS 100TeV

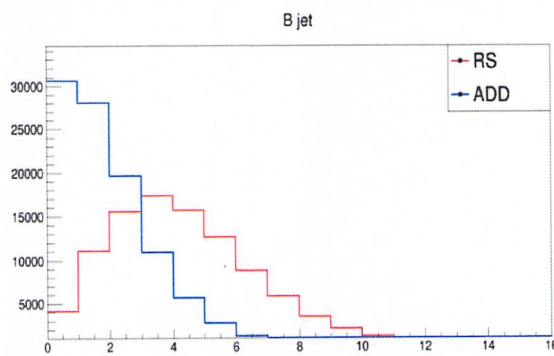
FIG. 10.3 Radiated particle type(Lepton)



(a) ADD 100TeV



(b) RS 100TeV



(c) ADD vs. RS 100TeV

FIG. 10.4 Radiated particle type(B-jet)